Review Article

Magnetic Nanoparticles-Loaded Poly(Methyl Methacrylate) Bone Cements for Magnetic Hyperthermia Treatment of Bone Tumors: State-of-the-Art Review

ABSTRACT

Background: Among emerging modalities for the treatment of bone cancers is magnetic hyperthermia treatment (MHT), which, it has been envisaged, will be used as an adjuvant to either of the two well-established ones surgery and radiotherapy). MHT involves intratumoral or systemic delivery of a suspension of MNPs to the tumor site, and, then, subjecting the site to an externally-generated alternating magnetic field for, typically, 30-60 min. In the recent literature, several shortcomings of MHT have been highlighted, which has led to the proposal of use of a variant of MHT that involves intratumoral injection of a suspension that includes a dough of a MNPs-loaded poly (methyl methacrylate) bone cement (MNPBC) to the site. A review of the literature on MNPBCs is lacking.

Purpose: The present contribution is a comprehensive and critical state-of-the-art review of the literature on MNPBCs.

Methodology: Through an exhaustive search of relevant databases, such as MEDLINE, Google Scholar, and PubMed, articles on MNPBCs published in the English language literature were identified, read, evaluated, and summarized. This allowed many topics to be covered in the present review, among which are characterization of the MNPs used to prepare various formulations of the cement, characterization of the cement formulations, and shortcomings of the literature. The last-mentioned aspect led to recommendations of thirteen topics for future study.

Conclusions: Among the topics recommended for future study are development of a testing standard for determination of *in vitro* properties of MNPBCs, performance of large-scale parametric studies on an appropriate animal bone tumor model (such as the influence of tumor size, tumor location, shape of the MNPs, and the magnitude and frequency of the applied magnetic field, on various measures of the heat-generation performance of an MNPBC), study of transient heat transfer involved in local MHT, and application of machine learning method(s) to determination of the heat-generation performance of an MNPBC.

Keywords: PMMA bone cement, magnetic hyperthermia

1. INTRODUCTION

Since its first use in 1958 in anchoring femoral head prostheses, poly (methyl methacrylate) (PMMA) bone cement has become one of the most widely used materials in orthopaedic surgery, with over 30 plain brands (formulations that do not include antibiotic(s)) and about 6 antibiotic-loaded brands approved for clinical use by regulatory agencies in a large number of countries, such as the US Food and Drug Administration and the European Medicines

Agency (EMA) [1-3]. As such, there is much information about the established uses of PMMA bone cements [1-3]. These uses are for primary and revision arthroplasties, delivery of antibiotic(s) to periprosthetic tissues in arthroplasties [1,3,4], filling a void created following curettage of a bone tumor [5,6], local delivery of chemotherapy and anti-infective drugs [7-9], and stabilizing a vertebral body (VB) following osteoporosis-induced vertebral compression fracture and restoring it to its original height (vertebroplasty or balloon kyphoplasty) [10,11]. Recently, another use of PMMA bone cement has been proposed, this being in a minimally-invasive treatment for cancer that is variously known as magnetic nanoparticle hyperthermia therapy, magnetic hyperthermia treatment (MHT), superparamagnetic hyperthermia treatment, magnetic induction hyperthermia, hyperthermic cancer therapy, and magnetothermal therapy [12-26].

The principle of MHT may be summarized as follows [27-45]. It involves intratumoral injection (or direct) or intravenous delivery of a magnetic colloid (comprising nano-sized magnetic particles (more commonly referred to as magnetic nanoparticles (MNPs) suspended in, for example, water) to the tumor site, and, then, subjecting the site to an externally-generated alternating magnetic field (AMF). With adequate amplitude and frequency of this field, the magnetization of the loaded MNPs is reversed, converting magnetic energy into thermal energy (heat). The generated heat is due to two phenomena: Néel relaxation (heat generation due to the rapid changes that occur in the direction of the magnetic moments without rotation of the NMPs) and Brownian relaxation (heat generation due to rotation of the MNPs). The generated heat leads to a temperature rise at the tumor site that is more rapid in the cancer cells than in the healthy tissue surrounding the tumor (“peri-tissue”). This is because cancerous tissues are poorly vascularized and, as such, cannot disperse heat, whereas the peri-tissue survives because it releases heat by increasing blood flow. A temperature rise of ∼4-8 ^{o}C above normal body temperature (that is, a temperature of between ∼41 ^{o}C and ∼45 ^{o}C) causes either gradual apoptosis or, even, necrosis of the cancer cells [46-49].

Both the theoretical attractions and shortcomings of HMT are well known [29, 31, 33, 35, 36, 37, 38, 39, 41, 43, 44, 45]. The advantages include ability to access both near- and deep-seated tumors, the large amount of the MNPs that reach the tumor site when direct delivery of the MNPs is utilized, and ability to specifically target tumor vasculature/hypoxic tumor cells. The shortcomings/challenges include a heterogenous distribution of the MNPs (and, hence, the temperature and, ultimately, the induced heat) in the tumor mass when direct delivery of the MNPs is used, the small amount of MNPs that reach the tumor site and the poor control of accumulation of the MNPs at the site when systemic delivery is used, the need to add extra constituent(s) to the MNPs when systemic delivery is used (which increases the cost of the procedure), leakage of the MNPs into the peri-tissues and the associated side effects, which include their postulated role in pathologies as disparate as Alzheimer’s disease and cardiovascular disease, high likelihood of overheating deep-seated tumors, uneven spatial distribution of the magnetic hyperthermia effect within the targeted cancerous tissue, limited penetration of the applied magnetic field into the body (limited to ∼50 mm, due to the loss of magnetic field gradient), and lack of validated guidelines on operational AMF parameters (namely, magnitude of field, frequency, and duration of application) that will ensure safe and effective MHT [31, 33, 35, 37, 38, 39, 41, 43, 44, 45]. All things considered, though, the current consensus is that a variant of MHT that involves intratumoral injection of MNPs (herein, referred to as “direct local MHT”) is a viable cancer treatment modality (especially as an adjuvant to either of the two most commonly used procedures of surgery and radiotherapy (RT) [50]). As such, there are many reports of the use of direct local MHT in clinical trials for treatment of various types of cancers [31, 51, 52, 53] and a few reports on its approved clinical use in a few countries for very limited use; for example, by the EMA for recurrent glioblastoma multiforme (in conjunction with RT) [35, 36, 44].

Loading the MNPs in an injectable medium that has a short liquid-to-solid transformation time *in vivo*, such as PMMA bone cement, avoids some of the drawbacks of direct local MHT, in particular, leakage of the MNPs. As such, recently, use of MNPs-loaded PMMA bone cement (MNPBC) to achieve local MHT has been receiving much research attention. It is envisaged that the steps in this method will be as follows. A powder mixture is prepared by blending the MNPs with the powder of a basis PMMA bone cement (control cement); the powder mixture and the liquid of the control cement are mixed and placed in a suspension, resulting in a suspension dough; the suspension dough is injected directly into the tumor site and, once the dough cures, the site is subjected to the AMF. There is now a sizeable literature on MNPBCs, with special reference to the feasibility of using them in direct local MHT of bone cancer. This choice of cancer is justified given that it has a low incidence but high morbidity, poor prognosis, and several intractable complications, such as hypercalcemia, bone deformity, and in the case of spinal metastatic tumor disease, collapse of VB(s) and progressive compression of the spinal cord. For example, in the United States, in 2023, there will be an estimated 4000 new cases of bone and joint cancers, an estimated 2140 deaths, a survival rate of ~55%, and ~300,000 adults living with metastatic bone cancer [54].

Using appropriate keywords, such as MNP, MHT, and MNPs-loaded PMMA bone cement, an exhaustive search of appropriate databases, such as Google Scholar, MEDLINE/PubMed, Embase, Web of Science, and CINAHL, was conducted for English language articles in the literature on MNPBCs and it was found that a review of this literature is lacking. Thus, the purpose of the present work is to address this shortcoming by presenting a detailed, comprehensive, and critical review of this literature. In the next six sections of this review, the focal aspects are methods used to synthesize MNPs that have been used in formulating MNPBCs (herein, referred to as, “relevant MNPs”), characterization of relevant MNPs, methods of preparation of MNPBCs, characterization of control bone cements (no MNPs are loaded) and of MNPBCs, shortcomings of the literature and suggested future studies to address these shortcomings, and a summary of the most salient points made in the review.

2. RELEVANT NANO-SIZED MAGNETIC PARTICLES AND METHODS OF SYNTHESIS

Four MNPs have been used in various studies, these being Fe_3O_4 [12, 13, 14, 18, 20, 55], a bioactive and ferrimagnetic glass-ceramic (SC45) (composition: 24.7 wt./wt%SiO_2-13.5wt./wt.%Na_2O-13.5wt./wt.%CaO-3.3wt./wt.%P_2O_5-14.0wt./wt.%FeO-31.0 wt./wt.%Fe_20_3) [15, 19, 26, 56, 57], a commercially-prepared mixture of Fe_3O_4 and TiO_2 [21, 22], and $Zn_{0.3}Fe_{2.7}O_4$ [24, 25].

For Fe_3O_4, in some studies, a commercially-available powder was used [12, 13, 18, 20, 21, 22, 55], but, in all the other studies, Fe_3O_4 particles were synthesized in-house using an oxidation precipitation method (OXP) [13], or a co-precipitation method (COP-A) [13], or a chemical co-precipitation method (COP-B) [14], or a modified co-precipitation method (COP1) [13].

In the synthesis of SC45, two methods were used, namely co-precipitation and traditional melting [15, 56, 57]. In the first of these studies (co-precipitation + melting method) [56], a mixture of $NaNO_3$, $Ca(NO_3)_2.4H_2O$, $(NH_4)_2HPO_3$, $FeSO_4.7H_2O$, $Fe(NH_4)(SO_4)_2.12H_2O$, and a colloidal SiO_2 solution was prepared; the resulting precipitate was dried in an oven, grounded, and heated in a furnace (air; 900 ^oC; 3 h); the resulting powder was melted in a Pt crucible (air atmosphere; melting temperature (T_{melt}) = 1400 ^oC – 1550 ^oC; 8.5 ^oC min^{-1}; 30 min); and, then, the resulting melt was poured onto a Cu plate. In the second study (traditional melting method) [57], a mixture of Na_2CO_3, $CaCO_3$, SiO_2, $CaHPO_4.2H_2O$, $FeSO_4.7H_2O$, and Fe_2O_3 was melted in a Pt crucible (air atmosphere; T_{melt} = 1400 ^oC – 1550 ^oC; 8.5 ^oC min^{-1}; 30 min) and, then, the resulting melt was poured onto a Cu plate. In the third study [15], a variant of co-precipitation + melting method was used.

For $Zn_{0.3}Fe_{2.7}O_4$ NPs, zinc (II) acetylacetonate, iron (III) acetylacetonate, sodium oleate, and oleic acid were mixed with benzyl ether in a flowing Ar atmosphere; the mixture was stirred with a magnetic stirrer, also in an Ar atmosphere and heated to 120 ^oC for 1 h; the mixture was further heated to a reflux temperature (300 ^oC) under an Ar blanket and kept at that temperature for 1 h; and, finally, after cooling down to 30 ^oC, the resulting MNPs were collected by centrifugation [24,25].

3. CHARACTERIZATION OF MAGNETIC NANOPARTICLES

Size, phase composition, morphology

These properties were obtained using an assortment of methods, such as x-ray diffractometry (XRD), scanning electron microscopy (SEM) without or with attached energy dispersive x-ray spectroscopy (EDS), and transmission electron microscopy (TEM) [56, 57, 58, 12, 13, 14, 15, 18, 21, 22, 24, 25].

For XRD, the settings used were CuKα radiation [14, 15, 21, 22, 56, 57] or Ni-filtered CuKα radiation [12, 13]; voltage of 40 kV [12, 13, 22]; current of 15 mA [22] or 40 mA [12, 13]; 2θ scanning rate of 2^o min^{-1} [12, 13, 22]; sampling angle of 0.01^o [22] or 0.02^o [12, 13, 15]; and scan step time of 1 s [15]. The crystalline phases were identified using a computer package in conjunction with a well-established database (2002 JCPDS-International Center for Diffraction Data) [15].

For Fe_3O_4, regardless of the method of synthesis, XRD results verified it to be 100% magnetite [12, 13, 14]. On the other hand, the synthesis method exerted a marked influence on the other properties determined. Thus, a commercially-available product (for example, REA powder) comprised cubic crystals, with size of 300 ± 200 nm [13] or mean size of $\sim$10 nm [14] but for in-house-synthesized powders (that is, OXP, COP-A, and COP-1 powders), the particles were nearly spherical, with size of 35 ± 15 nm, 11.5 ± 3.6 nm, and 5 ± 3 nm, respectively [13].

XRD patterns confirmed that the traditional melted-SC45 MNPs had a crystalline phase (comprising hematite and magnetite) embedded in an amorphous glass matrix, with the phase being well dispersed throughout the matrix [15, 56]. For T_{melt} between 1400 ^oC and 1500 ^oC, as T_{melt} increased, the amount of hematite decreased while that of magnetite increased. However, with T_{melt} of 1550 ^oC, the main crystalline phase was magnetite in an amorphous matrix. Over the full range of T_{melt} (1400 – 1550 ^oC), the amount of the magnetite phase increased non-monotonically with increase in T_{melt}, it being 36, 39, 46, and 42% when T_{melt} was 1400, 1450, 1500, and 1550 ^oC, respectively [56]. For SC45 MNPs synthesized using a traditional melting method, the size of the magnetite phase increased monotonically with increase in T_{melt}, this being 56, 59, 79, and 83 nm when T_{melt} was 1400, 1450, 1500, and 1550 ^{o}C, respectively [57]. Furthermore, the magnetite content of this MNP was determined to be 27.6% and 15.6% from XRD and calorimetric test measurements, respectively [15].

In the case of the powder comprising a mixture of Fe_3O_4 and TiO_2 [21, 22], the Fe_3O_4 powder comprised single-phase magnetite and the particles were spherical (diameter ~50 – ~100 nm) whereas the TiO_2 powder was a mixture of mostly anatase phase and a small amount of rutile phase and the particles were irregular in shape [21, 22].

The $Zn_{0.3}Fe_{2.7}O_4$ particles were polyhedral in shape, homogeneous in size, monodisperse with a narrow size distribution (~16 – ~22 nm; 21.8 ± 2.0 nm), single-crystalline (lattice fringes having a spacing of 0.29 nm, consistent with those of iron ferrite), and had a spinel structure [24, 25].

Specific power loss

This property was determined using calorimetry, but two approaches were taken [15, 56, 57]. In one approach, a magnetic induction furnace was used (40 kA m^{-1} (503 Oe); 440 kHz) [56, 57]. Small pieces of the MNPs (mass, m_c = 0.05 – 0.01 g) were immersed in 20 mL of water (hence, mass of water, m_w = 20 g) in a polymeric container and the initial temperature of the water (T_i) was measured, after which the cylinder was placed at the center of the coil of the furnace and an alternating magnetic field (AMF) (34 kA m^{-1} (43 mT or 430 Oe)) was applied to it for 2 min (t_a). Then, the power was switched off, the container was shaken to equilibrate the water temperature, and the final temperature of the water (T_f) was measured. Specific power loss (SPL) was calculated using the expression:

$$SPL = [m_w C_w (T_f - T_i)]/(t_a m_c),$$

where C_w is the specific heat of water (taken to be 4200 J/(kg.K).
Regardless of the method used to synthesize SC45 NMPs (traditional-melted or co-precipitation + melting), SPL increased non-monotonically with increase in T_{melt} [56,57].

In the other approach, a calibration test was first run and, for this, points were obtained during heating cycles applied to a specimen (fabricated using a mixture of pure magnetite (0, 25%, 50%, 75%, or 100%) and the MNP), immersed in 10 mL of distilled water, while in an induction furnace (15.1 kA m^{-1} (19 mT or 190 Oe) or 1 kW) for 3 min. The temperature of a specimen was recorded prior to and after the end of the test; hence, ΔT was obtained [15]. Calibration test results yielded the following correlation between ΔT and $\%Fe_3O_4$:

$$\Delta T = 0.2672 + 0.1233\ (\%Fe_3O_4) + 0.0021\ (\%Fe_3O_4)^2 \qquad R^2 = 0.9975$$

After the calibration test, calorimetric measurements were made using the same steps as used in the calibration test (with some changes) using specimens of three MNPBC formulations (P10, P15, and P20). Thus, now, the applied magnetic field (AF) varied between 14.3 and 37.4 kA m^{-1} (18 and 47 mT), the frequency of the field was 200 kHz, and the final cement specimen temperature was recorded 2, 4, 6, 8, 10, and 12 min after application of the field (t). For a given combination of MNPBC formulation and t, the variation of SPL with AF was of a power type; for example, for P20 at t = 240 s,

$$SPL\ (\text{in W } g^{-1}) = 0.0004(AF)^{2.4036} \qquad R^2 = 0.9922$$

At AF = 37 kA m^{-1} (47 mT) and t = 240 s, SPLs for P10, P15, and P20 were 2.3, 3.2, and 4.0 W g^{-1}, respectively.

Magnetic properties

These properties, which were obtained from the magnetization hysteresis curve (Figure 1) were determined, at room temperature, using a vibrating sample magnetometer (VSM) or a superconducting quantum interference device magnetometer, frequency of between 80 Hz and 430 kHz, and AF between 9.5 kA m^{-1} (120 Oe) and 955 kA m^{-1} (12,000 Oe) [12, 13, 14, 25, 56, 57].

For Fe_3O_4 powder, its saturation magnetization (M_s) and coercive force (H_c) varied with method of preparation [12, 13, 14]. For example, for REA, M_s was between 83 and 87 A m^2 kg^{-1} (83 and 87 emu g^{-1}) (close to that of bulk magnetite (89-95 A m^2 kg^{-1}) (89-95 emu g^{-1})) and H_c was 11.1 kA m^{-1} (140 Oe) whereas for powder synthesized by a co-precipitation method, M_s and H_c were 43.9 A m^2 kg^{-1} (43.9 emu g^{-1}) and 1.1 kA m^{-1} (14.2 Oe), respectively [12, 13, 14].

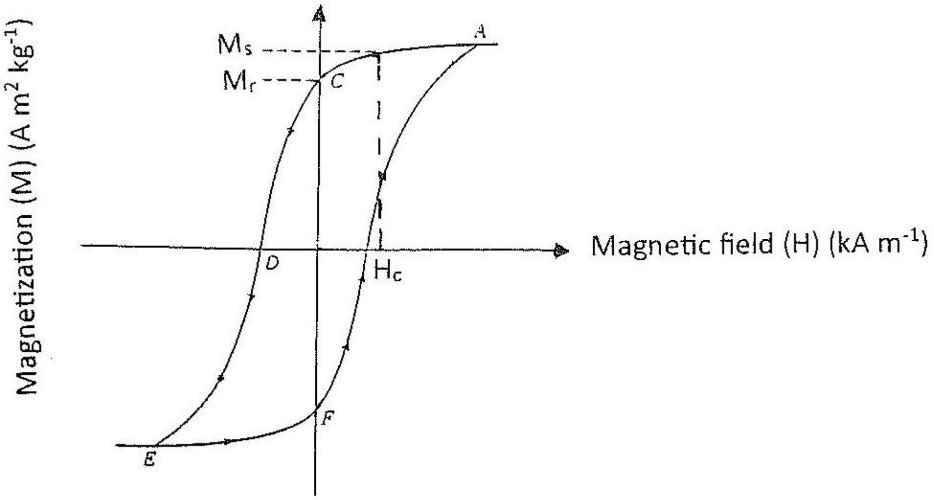

Figure 1. A schematic drawing of typical magnetization hysteresis curve.
M_s: saturation magnetization; M_r: remanent magnetization; H_c: coercive field. Note that for a nano-sized magnetic particle, the hysteresis loop (ACDEFA) is very narrow.

For SC45 MNPs, the magnetic properties depended on the synthesis method. Thus, when the method was co-precipitation + melting, the MNPs exhibited the characteristics of a soft magnetic material, with M_s, remanence magnetization (M_r), and H_c each increasing non-monotonically with increase in T_{melt} [56]; with AF of ±40 kA m^{-1} (±500 Oe), the interpolated hysteresis area (A_{ih}) increased non-monotonically with increase in T_{melt}, but, with ±796 kA m^{-1} (±10,000 Oe), the increase was monotonic [56]. Traditional-melted SC45 also exhibited the characteristics of a soft magnetic material, but, with increase in T_{melt}, the increases in M_s, M_r, and H_c were monotonic, non-monotonic, and non-monotonic, respectively [57], and at each of the applied fields (±40 kA m^{-1} (±500 Oe) or ±796 kA m^{-1} (±10, 000 Oe)), A_{ih} increased non-monotonically with increase in T_{melt} [57].

For $Zn_{0.3}Fe_{2.7}O_4$, the hysteresis loop results showed that at room temperature, it is superparamagnetic [25].

4. PREPARATION OF BONE CEMENTS

Composition of Control Bone Cement

In one study, the control bone cement was a two-part paste formulation [55]. In one paste, the powder phase comprised Fe_3O_4 particles (mean size = 13 μm), SiO_2 powder particles (3 μm), and benzoyl peroxide (BPO), while the liquid phase was bis-a-glycidylmethacryate (BMA) and triethylene glycol dimethacrylate (TGDM) (powder phase/liquid phase ratio (PLR) = 9:1). In the other paste, the powder phase comprised Fe_3O_4 particles and SiO_2 particles and the liquid phase was BMA, TGDM, and N,N-dimethyl-*p*-toluidine (DMPT) (PLR = 9:1). In preparing the cement, the two pastes were mixed. Five variants were formulated, with the amount of Fe_3O_4 particles in the powder being in the weight ratios of 10, 20, 40, 50, and 80%.

In each of the other studies, for the control cement, the powder constituents were PMMA beads (spherical, with mean size of 5 μm and mean molecular weight of 270 kg mol^{-1}) and benzoyl peroxide (BPO) (initiator)) [12, 13] or PMMA beads (spherical, with mean size of 38 μm) [14] or PMMA beads (spherical, with mean size of 4 μm and mean molecular weight of 270 kg mol^{-1}) and BPO [21, 22] or were those of a cement brand approved for clinical use in cemented arthroplasties (namely, Palamed® [15, 19, 26] or Osteopal® [20] or Palacos® MV [23]) or those of a commercially-available brand [24]. In these studies, the liquid constituents were methyl methacrylate (MMA) and DMPT [12, 13, 21, 22] or MMA [14], or those of Palamed® [15, 26], or of those of Osteopal® [20], or a mixture of MMA and the MNPs ($Zn_{0.3}Fe_{2.7}O_4$ particles) (hereafter designated, "modified control cement liquid") [24, 25]. The powder/liquid ratios used were 0.667 wt./wt.% [12, 13, 18], or 2 g mL^{-1} [15, 19, 23, 26], or 2.6 g/mL [20]. The mixing times used were 30 s [15, 16] or 3 min [12, 13, 21, 22].

Preparation Procedure

Three approaches were taken to preparing an MNPBC. In the most widely used approach, the MNPs were blended with the powder of the control cement and, then, the blend was mixed with the liquid of the control cement. The relative amounts of control cement powder, MNPs, and control cement liquid were given in a variety of formats, most commonly wt./wt.% or g mL^{-1} (Table 1). In the second approach, the modified control cement liquid was mixed with the control cement powder [24, 25]. The third approach involved prepared two variants of the MNPBC (aligned variant and random variant). To prepare the aligned variant, the modified control cement liquid was poured into a cylindrical Al_2O_3 mold and, then, a dc magnetic flux density of 1592 kA m^{-1} (20,000 Oe or 2 T) was applied along the axis of the mold for 40 min (by which time the cement was cured). For the random variant, no field was applied to the mold.

Table 1. Compositions of the PMMA bone cements

Study by Kawashita et al. [12]

Cement identifier	Powder mixture constituents (wt./wt.%[a])			Liquid constituents (wt./wt.%[b])	
	PMMA beads	BPO[c]	Fe_3O_4	MMA[c] monomer	DMPT[c]
Control	40	4[b]	0	60	2[d]
M-40c	24	4[b]	40	36	2[d]
M-50c	20	4[b]	50	30	2[d]
M-60c	16	4[b]	60	24	2[d]

[a] Relative to total mass of powder mixture.
[b] Relative to total mass of liquid constituents.
[c] BPO: benzoyl peroxide; MMA: Methyl methacrylate; DMPT: dimethyl-*p*-toluidene.
[d] Relative to mass of MMA.

Study by Li et al. [13]

Cement identifier	Powder mixture constituents (wt./wt.%[a])			Liquid constituents (wt./wt.%[b])	
	PMMA beads	Benzoyl peroxide	Fe_3O_4	MMA monomer	DMPT
C-PMMA	40	4[b]	0	60	2[c]
C-REA50	20	4[b]	50	30	2[c]
C-REA30	28	4[b]	30	42	2[c]
C-OXP50	20	4[b]	50	30	2[c]
C-COP30	28	4[b]	30	42	2[c]
C-COP30a	28	4[b]	30	42	2[c]

[a] Relative to total mass of powder mixture.
[b] Relative to total mass of liquid constituents.
[c] Relative to mass of MMA.

Study by Tang et al. [14]

Cement identifier	Powder mixture constituents (g)		Control cement liquid (mL)
	Control cement powder	Fe_3O_4	
PMMAc	20	0	10
PF-10	18	2	10
PF-20	16	4	10
PF-30	14	6	10

Studies by Bruno et al. [15], Miola et al. [19], and Miola et al. [26]

Cement identifier	Powder mixture constituents (g)		Control cement liquid[b] (mL)
	Control cement powder[a]	SC 45 glass ceramic	
Palamed (Control)	40	0	20
P10	36	10	20
P15	34	15	20
P20	32	20	20

[a] PMMA beads (32.28 g)+ ZrO_2 (5.28 g) + BPO (0.44 g) (Heraeus Kulzer Srl, Germany).

[b] MMA monomer (19.57 mL)+ DMPT (0.43 mL) +hydroquinone + E141 (chlorophyll colorant) (0.4 mg) (Heraeus Kulzer).

Study by Ling et al. [18]

Cement identifier	Powder mixture constituents (wt./wt.%)		Control cement liquid (wt./wt.%)
	Control cement powder	Fe_3O_4	
PMMA-0	40	0	60
PMMA-5c	38	5	57
PMMA-10c	36	10	54
PMMA-15c	34	15	51

Study by Yu et al. [20]

Cement identifier	Powder mixture constituents (g)		Control cement liquid[b] (mL)
	Control cement powder	Fe_3O_4	
PMMA	2.6	0	1
PMMA-3%Fe_3O_4	2.6	0.1095	1
PMMA-6%Fe_3O_4	2.6	0.2260	1
PMMA-9%Fe_3O_4	2.6	0.3560	1

Studies by Kubota et al. [21, 22]

Cement identifier	Powder mixture constituents[a] (wt./wt.%)			Liquid[b] (wt./wt.%)
	PMMA	Fe_3O_4	TiO_2	
M0T0	40	0	0	60
M10T10	32	10	10	48
M15T15	28	15	15	42
M20T20	24	20	20	36
M25T15	24	25	15	36
M30T15	22	30	15	33

[a] The mass ratio of benzoyl peroxide/MMA = 0.04

[b] The mass ratio of dimethyl-*p*-toluidene/MMA = 0.02.

Study by Ozdemir et al. [23]

Cement identifier	Powder mixture constituents (g)		Powder/liquid (g/mL)
	Control cement powder	Magnetic glass ceramic	
Control	3.0	0	2:1
P10	2.7	0.3	2:1
P20	2.4	0.6	2:1
P30	2.1	0.9	2:1
P40	1.8	1.2	2:1

Structural, morphological, and compositional properties

Scanning electron microscopy without or with attached energy dispersion spectroscopy and transmission electron microscopy were used to determine these properties [12, 15, 18, 21, 22, 24, 25].

For one Fe_3O_4 MNPs-loaded cement (M-40c, M-50c, and M-60c formulations), cross-sectional zones of the specimens showed uniform microstructure and uniform distribution of the Fe_3O_4 particles in the cement matrix [12].
For another Fe_3O_4 MNPs-loaded bone cement (PMMA-5c, PMMA-10c, and PMMA-15c formulations), the Fe_3O_4 nanoparticles were distributed evenly in the cement matrix and each of the relevant elements (C, O, and Fe) was well dispersed in the matrix [18].
For a third Fe_3O_4 MNPs-loaded bone cement (6 wt./wt.% loading) [20], the Fe_3O_4 particles were also uniformly distributed in the cement powder, with no agglomeration and good dispersion of them in both the solid and liquid phases of the cement.

For SC45 MNPs-loaded bone cement, (P10, P15, and P20 formulations), the surface of a specimen showed the presence of the SC45 powder and ZrO_2 particles (radiopacifier) well dispersed between the PMMA beads [15]. Cross-sectional zones of P10, P15, and P20 cement specimens showed the presence of the SC45 powder and ZrO_2 aggregates dispersed in the cement matrix as well as magnetite crystals [15].

For specimens of Fe_3O_4 + TiO_2-loaded MNPBC (M10T10, M15T15, M20T20, M25T15, M30T15 formulations) [21], there were dense structures, no macropores, fine particles of Fe_3O_4 and TiO_2 (except in MOTO formulation (control cement)), and micron-sized particles of PMMA particles, with the last-mentioned entities being markedly evident in formulations containing $\geq$ 40 wt./wt.% MNPs (namely, M25T15 and M30T15 formulations).

For 1 wt./wt.% $Zn_{0.3}Fe_{2.7}O_4$ MNPs-loaded cement formulation specimens, the Zn and Fe were uniformly dispersed in the cement matrix [24].

Porosity

Micro-computed tomography (μCT) (50 kV-800 mA x-ray source; exposure time of 5.2 s per projection; 3D reconstruction of a specimen; 3D visualization of the reconstructed specimen by means of commercially-available software packages; and volume of interest: 6.5 mm x 6.5 mm x 6.6 mm) was used to determine porosity of specimens of control cement and one SC45 MNPs-loaded cement formulation (P20 formulation) following fracture in a four-point bend test [15]. Porosity of P20 cement specimens was greater than that of the control cement [15].

Injectability

Two methods were reported on the determination of this property.

For the first method, the prepared dough of the cement (a Fe_3O_4 MNPs-loaded cement formulation) was injected into a 2-mL syringe, which was then placed into water and the progress of the resulting liquid-solid phase transformation was observed [18]. Although, in the report, pictorial information was given of this process, a quantitative result for injectability was not given.

With the other approach, the “injectable percentage” method [20, 59] was used. The cement dough of another Fe_3O_4 MNPs-loaded cement formulation (initial dough volume = V_{in}) was injected into a syringe (diameter = 1.2 mm), which was then positioned in a universal materials testing machine, and a compressive force of 3 kN was applied to the syringe, at a crosshead displacement rate of 15 mm min^{-1}. The test was terminated when either the force reached 70 N or practically all of the dough had been forced out of the syringe. The injection percentage was calculated using the expression:

$$\text{Injectable percentage (IP)} = 100\,[1-V_{le})/(V_{in}],$$

where V_{le} is volume of injected cement dough left in the syringe at end of the test (at least, 1 mL).

Control cement and each of three MNPBC formulations (PMMA-3%Fe_3O_4, PMMA-6%Fe_3O_4, and PMMA-3%Fe_3O_4) showed comparable and good injectability (IP= 90-97%) and among the MNPBC formulations, IP increased monotonically with increase in the Fe_3O_4 MNPs content.

Setting time and maximum polymerization temperature

Three methods were used to make the determination of these properties. One involved pouring the cement dough into a cylindrical poly(tetrafluoroethylene) (PTFE) mold; using Vicat needle to raster the surface of the cured cement in the mold, for 30 s; and, finally, recording the time it took for the needle to disappear (t_d). Setting time (t_{set}) was defined as the time between start of mixing of the cement and t_d [12].

The second method, which was used in four studies [14, 19, 20, 21], involved following the protocols stipulated in ISO 5833 [60]; that is, pour the cement dough into a PTFE mold and record the temperature of the curing cement as a function of time since commencement of mixing. The steps used to obtain t_{set} and the maximum exotherm temperature (T_{max}) from this record are given in the Standard.

The third method involved use of dynamic mechanical analyzer [26]. An indenter connected to a force transducer was immersed in the curing bone cement dough contained in a PTFE cylinder. The test was run at a frequency of between 5.00 Hz and 5.25 Hz, allowing a plot of the storage modulus (E') versus time during curing (t) to be obtained. t_{set} was defined as the time at which the maximum E' occurred. A thermometer, which was placed in contact with the cement specimen, was used to record the temperature of the curing dough, as a function of t, thus allowing T_{max} to be obtained.

For each of three Fe_3O_4 MNPs-loaded cement formulations (M-40c, M-50c, and M-60c formulations), t_{set} was shorter than (M-40c) or about the same as (M-50c), or longer than (M-60c) than that for the control cement. Among the MNPBC formulations, t_{set} increased monotonically with increase in the amount of Fe_3O_4 particles in the cement (Fe_3O_4 content) [12]. For each of these formulations, T_{max} was lower than that for the control cement and, among the formulations, T_{max} decreased monotonically with increase in Fe_30_4 content [12].

In the case of another Fe_3O_4 MNPs-loaded cement (PF-10, PF-20, and PF-30 formulations), t_{set} was longer than that for the control cement and among the formulations, t_{set} increased monotonically with increase in Fe_3O_4 content [14]. Among these cements, the difference in T_{max} for control cement and each of the MNPBC formulations was marginal [14].

For PMMA-3 wt./wt.%Fe_3O_4, PMMA-6 wt./wt.%Fe_3O_4, and 9 wt./wt.%Fe_3O_4 MNPBCs, t_{set} for an MNPBC formulation was marginally higher than that for the control cement (by between ~11% and ~14%) and among the formulations, t_{set} increased monotonically with increase in Fe_3O_4 content. The reverse trend was seen in T_{max}; namely, T_{max} for an MNPBC formulation was marginally lower than that for the control cement (by between ~6% and ~17%) and among the MNPBC formulations, T_{max} decreased monotonically with increase in Fe_3O_4 content [20].

For three SC45 MNPs-loaded cement formulations (P10, P15, and P20 formulations) [19, 26], t_{set} for a given formulation was between ~23 % and ~26% shorter than that for the control cement and among the formulations, t_{set} decreased monotonically with increase in the amount of SC45 MNPs in the powder (SC45 content) [26]. T_{max} for a given formulation was between ~6 % and ~10% lower than that for the control cement and among the formulations, T_{max} decreased non-monotonically with increase in SC45 content [26].

For five formulations of an MNPBC containing a mixture of Fe_3O_4 and TiO_2 MNPs [21, 22], t_{set} for a given formulation was longer than that of the control cement (by between ~44% and ~84%) and among the formulations, t_{set} increased monotonically with increase in the Fe_3O_4 + TiO_2 MPNs content (by between ~5% and ~28%). In contrast, T_{max} for a given formulation was lower than that of the control cement (by between ~5% and ~34%) and, among the formulations, T_{max} decreased monotonically with increase in the Fe_3O_4 + TiO_2 MNPs content (by between ~4% and ~31%).

A summary of t_{set} and T_{max} results for some of the cement formulations referred to above [12, 14, 19, 20, 26] is presented in Table 2.

Table 2. Summary of handling, and mechanical properties of the PMMA bone cements[a]

Cement	Setting time (min)	Maximum exotherm temperature (°C)	Compressive strength (MPa)	Flexural strength (MPa)	Flexural modulus (GPa)	Source [Ref.#]
Control	12.5 ± 1.0	95	85.3 ± 6.9			Kawashita et al. [12]
M-40c	11.2 ± 1.3	85	91.4 ± 6.1			
M-40c	12.5 ± 0.5	75	89.2 ± 6.5			
M-60c	14.5 ± 0.9					
Control	12.5 ± 1.0	95	83.5 ± 2.1			Li et al. [13]
C-REA50	12.5 ± 0.5	75				
C-COP30			86.0 ± 2.6			
Control	8.0 ± 0.0	77	113.7 ± 2.0			Tang et al. [14]
PF-10	11.3 ± 0.4	77	92.0 ± 1.7			
PF-20	17.8 ± 0.5	77	77.2 ± 2.2			
PF-30	22.0 ± 0.0					
Control			91	60	2.5	Bruno et al. [15]
P10			78	50	2.6	
P15			81	50	2.6	
P20			79	47	2.8	
Control	12.5 ± 1.0	48 ± 4				Miola et al. [19]

P10	11.9 ± 2.0	49 ± 3				
P15	12.0 ± 3.0	49 ± 2				
P20	12.2 ± 4.0	49 ± 2				
Control	5.0	60	83	75	2.1	Yu et al. [20]
PMMA-3%Fe_3O_4	5.3	59	81	65	2.3	
PMMA-6%Fe_3O_4	5.7	58	75	59	2.4	
PMMA-9%Fe_3O_4	6.0	26	58	50	2.6	
Control			75.5 ± 3.4	60.2 ±3.4		Ren et al. [24]
PMMA-1 wt.wt.% $Zn_{0.3}Fe_{2.7}O_4$			93.3 ± 6.3	72.2 ±2.3		
Control	7.70	84		58[b]; 55[c]		Miola et al. [26]
P10	5.95	79		51[b]; 56[c]		
P15	5.45	76		50[b]; 48[c]		
P20	4.95	76		48[b]; 46[c]		

[a] Presented either as mean ± population standard deviation or as mean.
[b] Determined with specimen at room temperature.
[c] Determined with specimen temperature = 37 °C.

Radiopacity

For SC45 MNPs-loaded cement [26], details of the method used were not provided. Additionally, the results did not give a straightforward comparison between the control cement and each of the three MNPBC formulations studied (P10, P15, and P20 formulations). Instead, a comparison was given of the radiopacity of one formulation (P20) that had been modified to contain only one radiopacifier (SC45 MNPs) (the other one, ZrO_2 having been removed) and the radiopacity of the control cement. No difference in the radiopacities of these two cements was found.

Magnetic resonance imaging

For the SC45 MNPs-loaded cements [26], small discs of a cement were placed on top of a cylindrical phantom containing water as the contrast agent. The cylinder contained a reference rigid structure of standard geometry that has clinical relevance; for example, its deformations are in the range of those recorded during taking of an magnetic resonance imaging (MRI) scan of a patient. A scanning system that is widely used in MRI of some parts of a patient (specifically, knee, ankle, calf, wrist, and elbow) (the O-Scan System®) was used to perform the scans. The applied magnetic field used was 247 kA m^{-1} (3100 Oe or 0.31 T). For each of the cement formulations, T1- and T2-weighted scans were performed on 18 sections of the phantom.

Only the images obtained in the central section of the phantom were included in the report because, it was emphasized, they were representative of all the images obtained at different distances from the surface. Two key results were 1) as expected, control cement specimens were not visible because the cement did not contain any magnetic material, no haloes were visible, and there were no differences between the T1- and T2-weighted images; and 2) in the case of an MNPBC formulation specimen, a dark halo was visible and the image became more and more deformed from the surface to the central sections. The results obtained in this study led to the conclusion that MRI may not be suitable for scanning patients after MHT in which SC45 NMPs-loaded cement was used.

Quasi-static compressive strength

This property was determined either using the protocol stipulated in ISO 5833 [60] or an in-house method.
When ISO 5833 was used [12, 13, 14, 15, 20, 21], universal materials testing machine was operated at a crosshead displacement rate (DR) of 20 mm min^{-1} [12, 13, 14, 15, 20, 21].
Alternatively, for the in-house method [24], the test cement specimens (diameter and height = 6 mm and 12 mm, respectively) were prepared, dried for 24 h at room temperature, before being tested in a universal testing machine using a DR that was not stated in the report [24].

For two formulations of one Fe_3O_4 MNPs-loaded cement (namely, M-40c and M-50c formulations), the compressive strength (σ_c) of each of the formulations was marginally higher than that of the control cement (mean increase of between ~5% and ~7%). Between the two formulations, σ_c decreased marginally (mean drop of ~2%) with increase of the amount of Fe_3O_4 MNPs (Fe_3O_4 particles content) [12] (Table 2). The first-mentioned trend was also found for the third formulation of this cement (C-COP30a formulation) (mean increase of ~3%) [13] (Table 2).

For another Fe_3O_4 MNPs-loaded cement, σ_c of each of two of formulations (namely, PF-10 and PF-20 formulations) was markedly lower than that of the control cement (drop of between ~15% and ~32%), and between the two formulations, σ_c decreased markedly (by ~16%) with increase in Fe_3O_4 content [14] (Table 2).

For three formulations of another Fe_3O_4 MNPs-loaded cement, σ_c of a given formulation was lower than that of the control cement (by between ~6% and ~32%) and among the formulations, σ_c deceased monotonically with increase in Fe_3O_4 content (mean decrease of between ~2% and ~27%) [20] (Table 2).

For SC45 MNPs-loaded composite cement, σ_c of each of the formulations (namely, P10, P15, and P20 formulations) was marginally lower than that for the control cement (by between ~11% and ~14%) [15] and among the formulations, the change of σ_c with increase in Fe_3O_4 content was very small (mean change between ~+4% and ~ –2%) and non-monotonic [15] (Table 2).

For Fe_3O_4 + TiO_2 MNPs-loaded cement, σ_c of some of the formulations was lower than that of the control cement (by between ~<1% and ~2%) but, for others, it was higher (by between ~1% and ~2%) [21]. Among the formulations, the trend of the variation of σ_c with Fe_3O_4 + TiO_2 content of the cement was complicated. It was concluded that these trends were consistent with the complex nature of the influence of cement composition on the bond strength between the powder mixture and the cement matrix.

For 1 wt./wt.% $Zn_{0.3}Fe_{2.7}O_4$ MNPs-loaded cement, σ_c was significantly higher than that for the control cement (93.34 ± 6.29 MPa versus 75.48 ± 3.45 MPa) [24] (Table 2).

Flexural strength and flexural modulus

These determined were using either the protocol stipulated in ISO 5833 (that is, four-point bend mode) [15, 20]) or an in-house method (bending mode not stated [24] or three-point bend [26]).

For three formulations of Fe_3O_4 MNPs-loaded cement [20], flexural strength (σ_b) of a given formulation was lower than that of the control (by between ~13 % and ~33 %) and among the formulations, σ_b deceased monotonically (mean of between ~8% and ~23%) with increase in Fe_3O_4 content [20]. For these cements, flexural modulus (E_b) of a given formulation was between ~9% and ~29% higher than that of control cement and among the formulations, E_b increased monotonically by between ~<1% and ~8% with increase in Fe_3O_4 content (Table 2).

For three formulations of SC45 MNPs-loaded composite cement, σ_b of a given formulation was lower than that of the control cement (mean decrease of between ~17% and ~22%) which, it was postulated, reflected the fact that SC45 particles introduced brittleness to the cement [15]. Among the formulations, there was a marginal but monotonic drop in σ_b with increase in SC45 particles content [15] and, regardless of the SC45 particles content, the fracture surface showed that the SC45 phase was well-dispersed in the cement matrix [15]. For these cements, the trends in flexural modulus (E_b) are the opposite of those for σ_b; namely, E_b of a given formulation was between ~4% and ~12% higher than that of the control cement and among the formulations, there was an increase of between ~<1% and ~8% with increase in SC45 content (Table 2).

In another report on three formulations of SC45 MNPs-loaded composite cement, the specimens (length, width, and thickness = 75 mm, 10 mm, and 3.3 mm, respectively) were prepared and tested in three-point bending (diameter of support roller = 5 mm; distance between support rollers= 30 mm) at DR = 1 mm min^{-1} [26]. Two sets of tests were conducted, with specimens being either in air while being tested (T_{test} = 22 ^oC) or maintained at 37 ^oC in a thermostatic bath for 5 min before being tested (T_{test} = 37 ^oC). Depending on the T_{test} used, some differences in the trends for σ_b were seen (Table 2). When T_{test} was 22 ^oC, σ_b of a given formulation was lower than that of the control cement (by between ~12% and ~18%) and among the formulations, σ_b decreased monotonically with increase in SC45 content in the powder. When T_{test} was 37 ^oC, σ_b for a given formulation was between ~3% higher and ~16 % lower than that for the control cement and among the formulations, σ_b decreased monotonically with increase in SC45 content in the powder. Regardless of the T_{set} value, fracture surfaces on the specimens showed cleavage and exposed particles of the radiopacifier (ZrO_2) (in both control cement and formulation specimens) as well as exposure of the SC45 particles (in formulation specimens). Thus, it was concluded that the difference in the σ_b trends at the two T_{test} values was unrelated to morphology.

For a 1 wt./wt.%$Zn_{0.3}Fe_{2.7}O_4$ MNPs-loaded cement, test specimens (length, width, and thickness = 75 mm, 10 mm, and 3.3 mm, respectively) were prepared and dried in air for 24 h. E_b of this cement formulation was markedly higher than that for the control cement (72.18± 2.30 MPa versus 60.22 ± 3.39 MPa) [24] (Table 2).

Dynamic mechanical properties (storage modulus, loss modulus, and loss factor)

Rectangular cement specimens of three SC45 MNPs-loaded cement formulations were used and the test was carried out using an in-house dynamic flexural analysis test setup [26]. The test was run with an oscillation frequency (f_o) that ranged between 2 Hz and 100 Hz, and the sinusoidal applied force (stimulus signal) and the accompanying sinusoidal specimen displacement (response signal) were fed to a software package that used them to calculate the storage modulus (E'), loss modulus (E''), and loss factor (= E''/E'), at a given f_o. Tests were run at 2 temperatures (T_{run}), namely, room temperature and 37 ^oC. At a given T_{run}, E' of a cement increased with increase in f_o, but the rate of increase decreased, tending to a plateau (at f_o of ~ 30 Hz when T_{run} was room temperature and ~ 70 Hz when T_{run} was 37 ^oC). At a given combination of cement, f_o, and T_{run}, E' for a given cement formulation was greater than that of the control cement. At a given T_{run}, the difference between the loss factor of a cement formulation and that of the control cement, over the whole range of f_o, was negligible. Thus, at room temperature, with $f_o > 22$ Hz, loss factor was independent of f_o and its mean value was ~0.08, and, at T_{run} = 37 ^oC, over the whole range of f_o used, loss factor was also independent of f_o, with its mean value was high (~0.10).

Residual monomer content

For this determination, the cement specimen was weighed and immersed in 5 mL of water in a screw bottle, kept for 7 d, at 37 ^oC, and, then, 10 mL of the lixiviums were analyzed using a liquid chromatograph [13]. Concentration of MMA in the lixivium was determined from a least-squares calibration line constructed using results from standard solutions containing 25, 50, 100, and 250 mg L^{-1} of MMA. The residual monomer content in specimens of one formulation of an Fe_3O_4 MNPs-loaded composite cement (namely, C-COP30a formulation) (mean = 2800 mg g^{-1}) was much higher than that in control cement specimens (mean = 1350 mg g^{-1}) [13]. This result was attributed to the powder/liquid ratio used in preparing C-COP30a cement specimens (1.38) being much larger than that used to prepare the control cement specimens (0.67) (Table 1), which resulted in retardation of the polymerization reaction [13].

In vitro apatite-forming ability

For five formulations of Fe_3O_4 + TiO_2 MNPs-loaded cement, this determination followed the standard protocol [61], which, among other things, involved immersing the test specimen in Kokubo's simulated body fluid (SBF) solution [62]. Two sets of key results were presented [22]. First, SEM images of surfaces of specimens of four of the formulations

(M15T15, M20T20, M25T15, and M30T15 formulations) showed that spherical structures similar to those of hydroxyapatite (HAp) were formed on each of them. Second, thin-film XRD patterns of the aforementioned surfaces contained diffraction peaks related to HAp. Thus, it was concluded that these two sets of results showed that each of these four formulations had excellent apatite-forming ability. Additionally, in the case of specimens of the control cement and the fifth formulation (M10T10), there no changes in the surface after a specimen had been soaked in the SBF (no surface occupancy of apatite).

In vitro bioactivity, toxicity, and biocompatibility/cytocompatibility/cytotoxicity

Bioactivity

For SC45 MNPs-loaded cement [16], the bioactivity test was performed in Kokubo's SBF solution [62]. On the surface of a test specimen, various aspects of the manifestation of bioactivity were observed, including the flat morphology of silica-gel (early stage), adsorption of Ca $^{2+}$ and PO_4^{3-} ions from the solution, and formation of a HAp layer. Thus, it was concluded that SC45 MNPs conferred bioactivity on the cement.

In another study on SC45 MPNs-loaded cement [23], bioactivity was also determined using Kokubo's SBF solution [62]. Prior to the test, the peaks in the EDS spectrum on a specimen surface were identified being C, O, and Zr (coming from the PMMA bone cement matrix) and Na, Ca, Si, and Fe (coming from the SC45 MNPs). After the end of the test, the P peak (which was very small prior to the test) and the Ca peak each increased, results that led to the postulate of the possibility of precipitation of $CaPO_4$ crystals, which was not uniform. It was concluded that these results suggest that the MNPBC was bioactive.

Toxicity

For SC45 MNPs-loaded cements [16], a leaching test was conducted on specimens of the cement formulation that had with the largest amount of SC45 MNPs (namely, P20 formulation) to determine the amount of iron released in a given time. A cement specimen was immersed in SBF, at 37 ^{o}C, for 30 d. At each of 6 time points (3 h, 1 d, 3 d, 7 d, 14 d, and 33 d), an aliquot of the solution was extracted and analyzed using a graphite furnace atomic absorption spectrometer (GF-AAS). The control cement was an approved bone cement brand (Palamed® MV) to which 20 wt.wt.% Bioglass® had been added to its powder. The measured iron released (0.6-1 mg L^{-1}) was about the limit of detection of the GF-AAS (0.3 mg L^{-1}) and was attributed to the iron in the saline buffer that used in the test and, more, importantly, was considerably less than the maximum daily concentration of iron that may be tolerated by a person (45 mg) [63]. Thus, it was concluded, that when used *in vivo*, it is unlikely that the MNPBC will result in iron overload.

Biocompatibility/Cytocompatibility/Cytotoxicity

Biocompatibility was determined for two formulations of an Fe_3O_4 MNPs-loaded cement (namely, C-PMMA and C-COP30a formulations) [13]. A cell suspension consisting of 50,000 rat fibroblast Rat-1 cells was seeded over the test cement discs positioned at the bottom of culture plates. Cell proliferation was examined after 1, 4, and 7 d of culture [13]. At each time point, this involved measuring the total DNA concentration from the incubated cells, at an absorbance of 260 nm, using a spectrophotometer. After Day 1, the difference between the biocompatibilities (expressed as total DNA, in ng mg^{-1}) of a composite cement formulation specimen (0.90 ± 0.05) and a control cement specimen (0.85 ± 0.05) was not significant. The same trend was found after Day 4 (respectively, 1.15 ± 0.1 and 1.15 ± 0.1). It was suggested that the results after Day 1 and Day 4 reflected the competition between the effect of residual monomer content (RMC) on the one hand and Fe_3O_4 nanoparticles on the other on Rat-1 proliferation on the discs; specifically, even though the RMC of a composite cement formulation disc was significantly higher than that of the control cement disc, the Fe_3O_4 MNPs in the formulation specimen retard Rat-1 cells. However, after Day 7, more Rat-1 cells adhered to composite cement formulation discs (total DNA = 1.35 ± 1.25 ng mg^{-1}) than on control cement discs (total DNA = 0.80 ± 0.10 ng mg^{-1}) [13], but the large scatter of the results from the composite cement discs makes statistical comparison between those results and those from the control cement discs problematic.

In a study on SC45 MPNs-loaded cement, human osteosarcoma-like cells (MG63) were cultivated in Dulbecco's Modification Minimal Essential Medium (DMEM) supplemented with 10% fetal bovine serum and 1% antibiotic (penicillin-streptomycin), at 37 °C, 5% CO_2 [16]. Two types of cytocompatibility tests, indirect and direct, were conducted. For the indirect test, cell viability was determined using a bromide-based colorimetric assay (MTT) and the optical density of the supernatant was measured, at 530 nm, using a spectrophotometer. The negative control was polystyrene. Cell morphology was determined using a light microscope and field emission SEM with attached EDS. For the direct contact cytocompatibility test, MG63 cells were seeded directly onto surface of a cement specimen and cell viability was determined using the assay and protocol as used for the indirect test. The results of both types of tests showed that cell morphology, adhesion, and density for the specimens of each of the composite cement formulations were each comparable to the corresponding result obtained with control bone cement specimens; namely, cells developed bridge-like complex structures (which, it was suggested, indicated pro-osteogenic activity) and, at time-point of 72 h, the cell organization had a tridimensional structure and several cells had a highly interconnected tissue-like multilayered network, all being features that, it was pointed out, are associated with enhanced pro-osteogenic activity. These features were much less evident in the control bone cement specimens. Thus, it was concluded that these results showed that whereas the composite cement formulation was bioactive, the control bone cement was bioinert. In addition, for a composite cement formulation, at each of the time points of 48 h and 72 h, a large amount of HAp crystals covered the cell surface which, it was suggested, pointed to synergism between the bioactivity and the cell activity of the formulation.

In another study on SC45 MNPs-loaded cement formulation (namely, P10 formulation), human fetal osteoblasts (hFOB) and MG63 cells were used as representative of non-tumor and tumor bone cells models, respectively [19]. For the cytotoxicity study, cell viability was evaluated using the MTT assay. The test was repeated after cells (hFOB or MG63) were seeded onto the surface of cement specimens, incubated for 24 h, and, then, the specimen was subjected to an AMF (magnitude = 18 kA m^{-1} (227 Oe)) for up to 30 min. For each combination of cement specimen and cell line, cell viability decreased with increase in time of exposure to the applied magnetic field, with the trend in the rate of decrease being the same for P10 cement specimen and hFOB, control specimen and hFOB, and control cement specimen and MG63 (drop from 100% to 70% in 30 min), whereas for the combination of P10 cement specimen and MG63, the drop was very steep (100% to 3% in 30 min; that is, by this time, almost all the cells had died).

For the cell proliferation study, a proliferating cell nuclear antigen (PCNA, PC10 rhodamine-conjugated sc-56) was used to detect early G1-proliferating and S phases-proliferating cells, with cement specimens observed under a fluorescent microscope, with the PCNA positive cells counted as means obtained from 20 random 1 mm^2 area/specimen. For each of the cell lines (hFOB and MG63), cell count after 48 h and the %annexin-5 positive cells (after 30 min) were each higher on P10 specimens than on control cement specimens (the latter result, it was pointed out, indicating cell apoptosis), but the difference in % PCNA positive cells on the two sets of specimens, for each of the cell lines, was small.

In a third study on three SC45 MNPs-loaded composite cement formulations (namely, P20, P30, and P40 formulations), human osteoblast (OBS) and U20S osteosarcoma cells were used [23]. After 3 d, cell attachment on the surface of a test specimen was observed using a fluorescence microscope and SEM. Cell viability was determined using a commercially-available assay (Alamar Blue®) for 1, 3, 7, 10, and 14 d in cell culture (t_{cult}). For a given cell line, on both control cement and composite cement formulation specimens, the cells spread out and extended their filopodia, connecting to each other. With increase in t_{cult}, cell viability on OBS was, essentially, invariant, whereas cell viability on U2OS increased monotonically. For a given combination of cell line and t_{cult}, the difference in cell viability between some pairs of cements was significant but not so for other pairs. For a given combination of cell line and cement specimen, cell viability decreased slightly with increase in t_{cult}. Using the criterion stated in ISO 10993-5 [64], which is that cell viability < 70% at t_{cult} = 3 d is deemed cytotoxic, control, P20, P30, and P40 composite cement formulations were cytotoxic for U20S cells at several values of t_{cul}, whereas, overall, none of the cements was cytotoxic for OBS cells at any value of t_{cul}.

For 1 wt./wt% $Zn_{0.3}Fe_{2.7}O_4$ MNPs-loaded cement, cytotoxicity was determined using mouse embryonic fibroblast cells [24]. Cell viability was determined using a commercially-available cell counting assay (CCK-8) and absorbance was measured, at 450 nm, using a multimode plate reader. It was found that cell viability on a composite cement formulation specimen was not significantly different from that on the blank control specimen or on the control cement specimen, demonstrating, it was concluded, that the composite cement formulation has no toxic effect on the cells and, as such, is biocompatible.

The results of the study on 0.2 wt./wt.% $Zn_{0.3}Fe_{2.7}O_4$ MNPs-loaded cement [25] were the same as those reported in the previous one [24].

Biosafety in animal tumor model

In a New Zealand White rabbit tibial plateau tumor model (VX2 solid tumor mass), cell apoptosis results, obtained from flow cytometry tests, gave an insignificant difference between the proportion of living cells in a group comprising 6 formulations of a Fe_3O_4 MNPs-loaded cement (92.04 ± 0.74%) and that in the control cement group (94.02 ± 0.80%) [20]. For each of the MNPBC formulations, there were no toxic effects, no inflammatory cells, no discernible damage in the tissues around the cement layer, and no effects on heart function, kidney function, and blood function. Thus, it was concluded, that the MNPBC was biocompatible and biosafe.

Magnetic properties

These properties were determined, in room temperature, using a VSM in an AMF, with AF ranging from 3.2 to 795.8 kA m^{-1} (40 Oe to 10,000 Oe) at a frequency (f) ranging from 80 kHz to 600 kHz.

For one formulation of an Fe_3O_4 MNPs-loaded cement (M-40c formulation), when AF = 9.6 kA m^{-1} (120 Oe), the area of the hysteresis loop was very small whereas, when H = 23.9 kA m^{-1} (300 Oe), the area was larger. The same trend was found for another formulation of the cement (M-50c formulation) [12]. With either test AF, the heat-generation potential (= area under the hysteresis loop) was larger for M-50c formulation than for M-40c [12].

For another Fe_3O_4 MNPs-loaded cement, under a given AF (9.5 or 23.9 kA m^{-1} (120 or 300 Oe)), the heat-generation potential of one formulation (C-REA50 formulation) was greater than that of each of two other formulations (C-REA30 and C-OXP50 cement formulations) [13]. Regardless of the test AF, another formulation of the cement (C-COP30 formulation) did not display a measurable hysteresis loop and, as such, no comment was made about its heat-generation potential. Thus, the conclusion was that these results for this formulation are consistent with the fact that it has superparamagnetic properties. These results, when taken in conjunction with those on M_s and H_c of the starting powders showed that the Fe_3O_4 particles retained their magnetic properties after being loaded in a MNPBC. Thus, for example, some of the MNPBC formulations (specifically, C-REA30, C-REA50, and C-OXP50 formulations) as well as the corresponding starting powders (REA and OXP) have large H_c values and, hence, display ferromagnetic properties.

With AF = 796 kA m^{-1} (10,000 Oe), each of three formulations of another Fe_3O_4 MNPs-loaded cement (PF-10, PF-20, and PF-30 formulations) have a low H_c (0.167 ± 0.048 kA m^{-1} or 2.1 ± 0.6 Oe or 2.1 ± 0.6 G), which it was suggested, indicated that each formulation possessed superparamagnetic properties [14].

For one formulation of another Fe_3O_4 MNPs-loaded cement (6 wt./wt.% Fe_3O_4), the hysteresis loop was narrow, indicating that it is a soft magnetic material, with M_s and H_c of 8.62 A m^2 kg^{-1} (8.62 emu g^{-1}) and 6.7 kA m^{-1} (84.45 Oe), respectively [20].

Each of three formulations of SC45 MNPs-loaded cement studied (P10, P15, and P20 formulations), M_s increased monotonically with increase in SC45 content in the formulation (1.6, 2.5, and 4.2 A m^2 kg^{-1} (1.6, 2.5, and 4.2 emu g^{-1})) for P10, P15, and P20, respectively) [19].

For five formulations of a composite cement comprising loaded Fe_3O_4 + TiO_2 MNPs (M10T10, M15T15, M20T20, M25T15, and M30T15 formulations), M_s increased monotonically with increase in its Fe_3O_4 content; specifically, M_s for M10T10, M15T15, M20T20, M25T15 and M30T15 (with the corresponding Fe_3O_4 contents being 10.0, 16.6, 18.9, 25.6, and 29.3 wt./wt.%, respectively) were 9.5, 16.2, 18.5, 25.0, and 28.7 A m^2 kg^{-1} (9.5, 16.2, 18.5, 25.0, and 28.7 emu g^{-1}), respectively [22]. In contrast, among these formulations, H_c value was, essentially, constant (9.23-9.88 kA m^{-1} (116-124 Oe)) [22].

It was found that 0.2 wt./wt.% $Zn_{0.3}Fe_{2.7}O_4$ MNPs-loaded cement is superparamagnetic and its M_s increased monotonically with increase in the size of the particles (D_p), ranging from 440 to 461 kA m^{-1} (5528 to 5792 Oe) with D_p ranging from 16 nm to 22 nm [25], this trend being attributed to the reduction of volume of canted surface spins with increase in D_p [65]. For this MNPBC, clear differences were exhibited when MNPs were randomly dispersed

(RD cement) compared to when they were aligned (AD cement [25]. Three of these differences are highlighted. First, with RD cement, the hysteresis loop was slanted, with a very small opening whereas with the AD cement, the loop was square, with a higher remanence ratio (= M_r/M_s). Second, at low temperature, the coercivity of AD cement was higher than that of RD cement, but at higher temperature (>100 K), the coercivities of the two variants were about the same. Third, the area of the hysteresis loop (= SLP value) of AD cement was much larger than that of RD cement. Explanations provided for these differences in the results are summarized thus. When an AMF was applied to AD cement during its curing, the MNPs produced long chains and these chains rotated to align their easy axes in the direction of the field, thereby minimizing the Zeeman effect. These two phenomena result in an increased remanence ratio and a narrower switching field distribution. In contrast, during testing of RD cement, the MNPs did not flip their magnetic moment, resulting in a magnetization that was nearly linear with change in H and, hence, the cement has a lower SLP. An additional result was that the enhancement ratio (ER) (= SLP for AD cement/SLP for RD cement) decreased monotonically with increase in AF; thus, ER = 50 and 1 when AF = 4 kA m^{-1} (150 Oe) and 27 kA m^{-1} (340 Oe), respectively.

In vitro heat generation properties

The majority of studies on this property involved subjecting a cement specimen to an AMF and recording the temperature of the surface of the specimen (T_{surf}) at a given time (t) over the duration of the application of the field [12, 13, 14, 15, 19, 20, 21, 22, 24]. In some of these studies, the T_{surf}-versus-t record was obtained (Figure 2) [12, 13, 14, 19, 20, 21, 22], but, in others, the record was of temperature rise (T_{surf} – initial temperature of the specimen) versus t [15, 24]. In each of these studies, T_{surf} was measured using a fluoroptic/fiber optic thermometer/probe or a thermocouple temperature probe or an infrared thermometer.

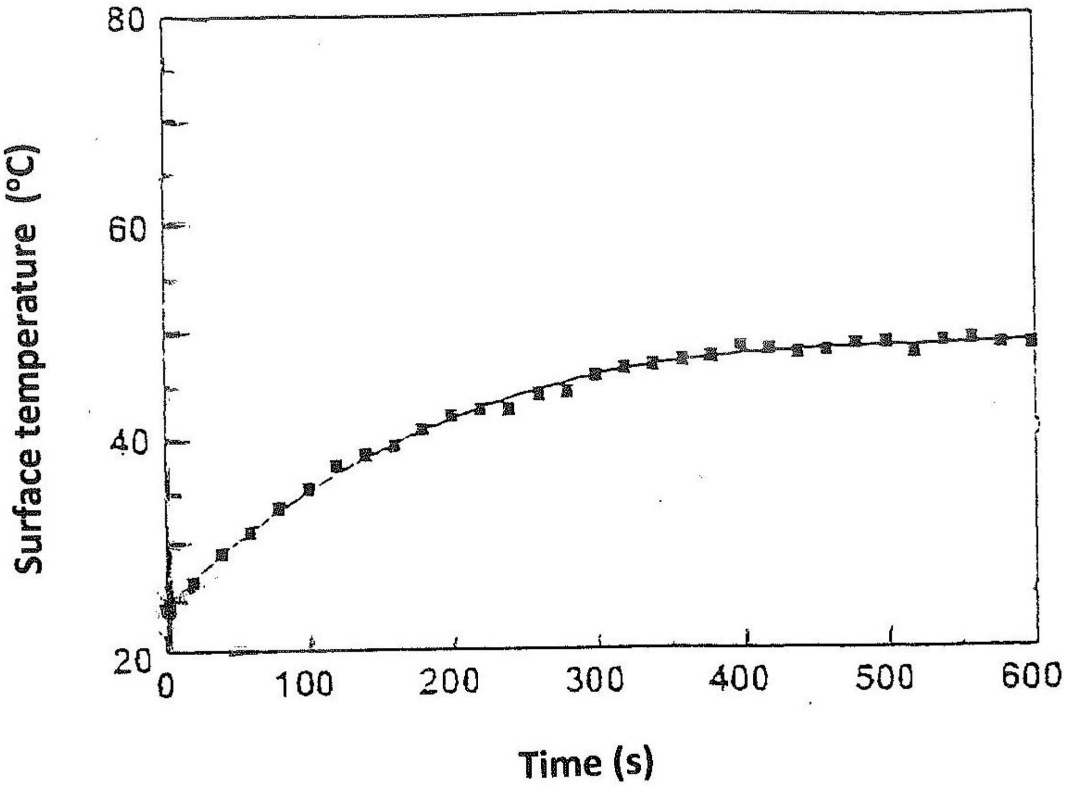

Figure 2. A schematic drawing of the results of determination of the heat-generation performance of an MNPs-loaded PMMA bone cement, for a set of test conditions (applied alternating magnetic field and frequency of application).

In two studies involving three formulations of SC45 MNPs-loaded cement, an alternative methodology was used to determine the heat-generation performance of the cement, this involving the use of a purpose-built calorimetry setup [15, 19]. A test cement specimen was placed in a tube, distilled water was put in it, and a polyethylene foam sleeve was wrapped around the tube. The tube was then subjected to an AMF (AF of up to 31.3 kA m^{-1} (393 Oe); f = 220 kHz) for up to 12 min, during which time the temperature of the surface of the tube (T_t) was measured. It was found that for a given combination of composite cement formulation and AF, T_t increased almost linearly with increase in t, a trend attributed to the effect of the foam band wrapped around the test tube.

Six key results or trends in the results for the heat-generation performance tests on specimens of the four MNPs used to formulate MNPBCs (namely, Fe_3O_4, SC45, Fe_3O_4 +TiO_2, and $Zn_{0.3}Fe_{2.7}O_4$) are now summarized.

First, In a study on an Fe_3O_4 MNPs-loaded cement, rectangular blocks of cement (20 mm x 20 mm x 20 mm (h)) were subjected to an AMF (AF = 6.4 kA m^{-1} (80 Oe) or 7.9 kA m^{-1} (100 Oe); f = 100 kHz) for up to 10 min and, then, the temperature of the block was measured [55]. The influence of the Fe_3O_4 content of the cement (C), the height of the cement block (h), and AF on the temperature of the block (T_{bl}) was determined. Some key trends in the results were 1) T_{bl} increased monotonically with increase in C (10 wt./wt.% $\leq$ C $\leq$ 80 wt./wt.%), with, for example, when C = 20 wt./wt.%, T_{bl} = 30 ^{o}C and when C = 60 wt./wt.%, T_{bl} = 45 ^oC; 2) T_{bl} increased monotonically with increase in h (5 mm $\leq$ h $\leq$ 20 mm), with, for example, when h = 13 mm, T_{bl} = 45 ^oC and when h = 20 mm, T_{bl} = 60 ^oC; and 3) T_{bl} increased monotonically with increase in AF (5.6 kA m^{-1} (70 Oe)) $\leq$ H $\leq$ 13.5 kA m^{-1} (170 Oe)), with, for example, when AF = 5.6 kA m^{-1} (70 Oe), T_{bl} = 25 ^oC, and when AF = 10.1 kA m^{-1} (127 Oe), T_{bl} = 45 ^oC.

Second, T_{surf} of control cement specimen is invariant with increase in t [12, 14, 15, 19, 20, 24] (that is, control cement did not possess heat-generating ability).

Third, for a given MNPBC formulation, with increase in t, T_{surf} increased rapidly at first and, then, the rate of rise decreased substantially, tending to a constant value [12, 13, 14, 15, 20, 21, 22, 24].

Fourth, for a given combination of MNPBC formulation, AF, f, and t, increase in C led to increase in T_{surf} [12, 13, 20].

Fifth, for a given combination of MNPBC cement formulation, f, and t, increase in AF led to a dramatic rise in T_{surf} [12, 13, 14].

Sixth, for a given combination of MNPBC formulation, f, t, and method of synthesis of Fe_3O_4 MNPs, AF exerted a noticeable effect on T_{surf}, although the trend was complicated [13].

It has been postulated that for local MHT to be a considered a viable clinical modality, T_{surf} of between ~41 and ~45 ^oC is needed [46-49]. Thus, a conservative approach would require T_{surf} of at least 45 ^oC (~8^o above normal body temperature). The combination of AF, f, and t that produces this requisite value of T_{surf}, for various composite cement formulations, is given in Table 3. Additionally, it has been suggested that in order to avoid overheating during local MHT, the product of the operational AF and f used must be < 5 x 10^6 kA m^{-1} s^{-1} (62.84 x 10^6 Oe s^{-1}) [33]. Applying these criteria to the data given in Table 3 leads to the selection of five MNPBC formulations that have high potential for use in local MHT; namely, M-50c, C-REA50, PMMA-3%Fe_3O_4, M30T15, and PMMA-0.2 wt./wt.%$Zn_{0.3}Fe_{2.7}O_4$ (aligned particles arrangement).

Table 3. PMMA-based composite bone cement formulations with potential for use in magnetic hyperthermia of bone cancers (based on results of *in vitro* tests)

Cement formulation	Applied magnetic field (Oe^a)	Frequency of field (kHz)	Duration of application of field (s)	Source [Ref. #]
M-50C	120	100	325	Kawashita et al. [12]
C-COP30	300	100	80	Li et al. [13]
C-COP30	400	100	48	
C-OXP50	120	100	180	
C-OXP50	400	100	110	
C-REA50	120	100	300	
C-REA50	400	100	250	

PF-10	150	500	100	Tang et al. [14]
PF-10	125	500	200	
PF-10	100	500	550	
PF-20	150	500	50	
PF-20	125	500	50	
PF-20	100	500	150	
P10	430	220	720	Bruno et al. [15]
P15	430	220	480	
P20	430	220	300	
PMMA-3%Fe_3O_4	72	626	70	Yu et al. [20]
PMMA-6%Fe_3O_4	72	626	30	
PMMA-9%Fe_3O_4	72	626	10	
M25T15	40	600	600	Kubota et al. [21,22]
M30T15	40	600	430	
PMMA-1 wt./wt.% $Zn_{0.3}Fe_{2.7}O_4$	176	430	180	Ren et al. [24]
PMMA-1 wt./wt.% $Zn_{0.3}Fe_{2.7}O_4$	226	430	80	
PMMA-1 wt./wt.% $Zn_{0.3}Fe_{2.7}O_4$	289	430	50	
PMMA-1 wt./wt.% $Zn_{0.3}Fe_{2.7}O_4$	339	430	40	
PMMA- 0.2 wt./wt.% $Zn_{0.3}Fe_{2.7}O_4$ (randomly oriented particles)	339	430	130	Yu et al. [25]
PMMA- 0.2 wt./wt.% $Zn_{0.3}Fe_{2.7}O_4$ (aligned particles)	50	430	140	
PMMA- 0.2 wt./wt.% $Zn_{0.3}Fe_{2.7}O_4$ (aligned particles)	126	430	80	
PMMA- 0.2 wt./wt.% $Zn_{0.3}Fe_{2.7}O_4$ (aligned particles)	176	430	75	
PMMA- 0.2 wt./wt.% $Zn_{0.3}Fe_{2.7}O_4$ (aligned particles)	339	430	60	

---

[a] Conversion to SI units: 1 Oe = 0.08 kA m^{-1}.

***Ex vivo* heat generation performance and related properties**

In a study involving a 50 wt./wt.% Fe_3O_4-loaded composite cement, the lower leg of a human cadaver that been stored at -30 ^{o}C was used [55]. After heating the medullary canal to 37 ^{o}C, a skin incision was made on the anteromedial aspect of the proximal tibial diaphysis and the skin, muscle, and periosteum were retracted. A rectangular window was made in the cortical bone, the bone marrow was completely removed and the cavity was filled with the cement (creating a cement plug), after which the surgical site was subjected to an AMF (maximum AF = 23.9 kA m^{-1} (300 Oe); f = 100 kHz) and, then, the temperatures on the surface of the cement plug, the outside surface of the bone, in the adjacent medullary canal 5 mm from the cement, and in medullary canal 10 mm from the cement were recorded. After 5 min, these temperatures were 63, 40, 38, and 38 ^{o}C, respectively [55].

There have been four other studies on this aspect, with these using excised vertebra from a cow [17], excised liver from a pig [18, 20] and excised rib from a pig [25].
In the first study, a dough of an MNPBC (an approved bone cement brand (VertaPlex®) loaded with Fe_3O_4 MNPs) was injected into a cylinder, and upon polymerization of the dough, the cylinder was inserted into a cylindrical hole created in the core of a beef vertebra. The specimen was immersed in distilled water and then placed ~10 cm above an alternating magnetic field generator [17]. The generator was turned on and the temperatures of the cement cylinder (T_{cyl}) and of the vertebral body (T_{sp}) were measured, as a function of time of application of the field (t). Many cycles of heating were applied. Two key trends in the results were 1) T_{cyl} increased with increase in t, reaching a maximum ~28 ^{o}C at t = ~2100 s and, then, decreasing with further increase in t to a final value of ~21 ^{o}C, whereas 2) T_{sp} increased very slowly with increase in t, reaching a maximum of ~21.5 ^{o}C at t = ~4800 s and, then, decreasing very slowly with further increase in t to a final value of ~21 ^{o}C at ~5500 s.

A study on another Fe_3O_4 MNPs-loaded cement involved injecting bone cement dough into a piece of an excised bovine liver (herein termed a liver block), subjecting the liver block to an AMF (f = 625 kHz, output current = 28.6 A, and coil diameter = 30 mm) and recording the surface temperature of the block (T_{surfbl}), as a function of time (t) up to 300 s [18]. Three key results were 1) for each of the four cements tested (control cement and three MNPBC formulations (PMMA-5c, PMMA-10c, and PMMA-15c)), the T_{surbl}-versus t profile was the same as that reported in *in vitro* tests; namely, for control cement, T_{surbl} was invariant with increase in t, whereas, for each of the MNPBC formulations, T_{surfbl} increased with increase in t, with T_{surbl} tending to a constant value at t of ~180 s and at a given t, T_{surbl} increased with Fe_3O_4 content of the composite cement formulation; 2) t at which T_{surbl} reached 45 ^{o}C was 20 s for the PMMA-15c liver block and 80 s for the PMMA-10c liver block; and 3) the end of the test (300 s), T_{surfbl} for PMMA-5c liver block had not risen to 45 ^{o}C. Based on these results, the authors selected PMMA-10c for the next stage in the study. This involved shaping the cement dough into an elliptical ball, allowing it to cure, and then, drying it for 24 h, and implanting it in a piece of excised bovine liver and, then, subjecting the piece to an AMF (conditions the same as stated above) for a given time (t′) (60 s ≤ t′ ≤ 240 s). After that, the piece was divided into two and the coagulation necrosis area (or ablation area) (S) was calculated. The results showed that S increased monotonically with increase in t′, the means being 1.24, 1.70, 2.76, and 4.17 at t′= 60, 120, 180, and 240 s, respectively).

In a study on 6 wt./wt.% Fe_3O_4-loaded cement formulation, a rectangular piece of excised bovine liver was filled with hemispherical balls of the cement (yielding a liver block) and, then, the liver block was subjected to a magnetic field for 3 min [20]. At a given time after commencement of the application of the field, the temperature of the block (T_{lb}) increased rapidly in the closed tissue but decreased with increase in distance from the surface of the liver block; for example, at time = 150 s, mean T_{lb} were 82.7, 53.8, and 36.9 ^oC, at positions 1, 2.5 mm and 5 mm from the surface, respectively. It was stated that results indicated that while the treated section experienced high temperature, surrounding healthy tissues were not heated. Ablated tissue distance was measured and found to increase monotonically with heating time, with means of 1.38, 3.06, and 4.82 mm after times of 120, 150, and 180 s, respectively.

In a study on two variants of 0.2 wt./wt.%$Zn_{0.3}Fe_{2.7}O_4$ z MNPs-loaded cement, a cylindrical hole was drilled into an excised rib of a pig and then the hole was filled with a dough of the cement (creating a cement plug) [25]. After the cement cured, the plug was subjected to an AMF (AF = 4 kA m^{-1} (50 Oe); f = 430 kHz) and the temperature of the surface of cement plug and of bone 7 mm from the center of the plug (T_7) was recorded. In the variant in which the MNPs were aligned, after 600 s, the surface of the plug reached 85 ^oC but T_7 reached 45 ^oC, but in the variant in which the MNPs were randomly dispersed, there was no measurable rise in the temperature at either location.

Heat-generation performance in an animal tumor-free model

In a study involving the two-paste Fe_3O_4 MNPs-loaded cement and Japanese White rabbits, a small skin incision was made in the patellar ligament and then the ligament was transected [55]. After reaming the medullary canal, a cylindrical plug of the 50 wt./wt.% formulation of this cement was inserted into the medullary canal. After the wound healed, the lower leg containing the cement plug was exposed to an AMF (AF = 7.9 kA m^{-1} (100 Oe); f = 100 kHz) for up to 58 min. After 40 min, on the surface of the cement plug, the interface between the bone and the muscle, and in the medullary canal, the temperatures were measured to be 50, 38-45, and 30 ^oC, respectively.

A rod of 2 wt./wt.% $Zn_{0.3}Fe_{2.7}O_4$ cement was implanted into the medullary canal of the tibia of New Zealand White rabbits and then the tibia was exposed to an AMF (AF = 4-25 kA m^{-1} (50-315 Oe); f = 380 kHz) and the temperature of the medullary canal (T_{mc}) was recorded, as a function of time (t) [25]. At a given AF, the rise in T_{mc} with t was considerably faster when the MNPs in the cement formulation were aligned than when they were randomly dispersed; for example, with AF = 9 kA m^{-1} (113 Oe) and t = 400 s, T_{mc} when aligned and randomly dispersed variants were used were 54 ^oC and 33 ^oC, respectively.

Heat-generation performance and related properties in an animal tumor model

Four studies have been reported on this aspect [18, 20, 24, 25].

In the first study, the MB-231 human breast cancer xenograft in nude mice was used [18]. After collecting the MB-231 cells, they were dispersed into DMEM cell culture medium and 100,000 of them were injected into the back of each mouse subcutaneously. After the tumor volume reached between 0.35 cm^3 and 0.55 cm^3 (this took 4 wk), the mice were divided into 2 study groups. The mice in Group 1 (n = 3) received no treatment for the inserted cancer xenograft whereas those in Group 2 (n = 6) received treatment, which involved anesthetizing the mouse and, then, injecting a ball of the MNP cement formulation (namely, PMMA-10c formulation) into the tumor tissues under real-time ultrasound induction and, then, using computed tomography to visualize the position of the cement ball. The mouse was then exposed to an AMF for 180 s, after which an infrared thermometer was used to record the surface temperature of the tumor (T_{tu}) for a time (t) of up to 180 s. 24 h after the treatment, 3 of the mice were euthanized and the microstructure of the ablated tumor was obtained. Three key results are summarized. One, T_{tu} increased with increase in t, with the pattern being the same as that reported in the *in vitro* studies [12, 13, 14, 15, 25] and *ex vivo* studies [12, 25]. Two, at t = 180 s, the skin on the tumor mass turned into a pale color but, with increase in the number of days after the magnetic field exposure (DAT) ($0 \leq$ DAT ≤ 15 d), the skin color darkened and, by DAT = 3, a scab began to form on the tumor tissue and, by DAT = 10, the scab began to desquamate and, by DAT = 15, the scab separated and fell off. Additionally, at a given DAT, in the case of Group 2 mice, the boundary between ablated and non-ablated tissue was clear. Three, with increase in DAT, the body weight of the mice in each of the two study groups remained stable, the volume of the tumor mass (V_{tu}) in the Group 1 mice increased continuously (rising from zero at the start of the test to 2.3 ± 0.4 cm^3 at Day 15), whereas in the Group 2 mice, V_{tu} decreased continuously, dropping to zero at Day 15.

In the second study, a New Zealand White rabbit tibial plateau tumor model (VX2 tumor mass) was used [20]. Using a very small coaxial puncture needle, the tumor mass was seeded in the tibial plateau and, after 13-15 d, the bone tumor volume had grown to 180 ± 15 mm^3 and was positioned in the central cancellous bone region of the plateau. An MNPBC formulation (6 wt./wt.% Fe_3O_4-loaded formulation) was injected into the tumor, after which the tumor-bearing leg of the rabbit was placed in a water-cooled magnetic induction coil and subjected to an AMF for up to 150 s. The surface temperature of the tibia was measured, as a function of time of exposure to the magnetic field. Two key results were 1) new bone formed in the absorbed area of the tibia after Day 42, showing that the heated area was well controlled; and 2) the magnetic field exposure eliminated the tumor mass completely with no accompanying large lesions in the surrounding healthy tissues.

In the third study, a New Zealand White rabbit tibial plateau tumor model (VX2 tumor mass) was used [24]. After fast thawing in warm water, a cryopreserved tumor mass was cut into a very small piece, collected by centrifugation, and re-suspended by phosphate buffered saline (PBS) solution. Following anesthetization of the rabbit, the tumor mass suspension was injected into muscles in its right hind leg. After 21 d, the tumor mass was excised and sliced into small pieces. A puncture point located 10 mm under the tibial medial plateau was made on the skin on the right hind leg of the animal, small tumor mass pieces were injected 30 mm into the bone marrow cavity of the tibia through a bone hole, a small volume of fluid was taken from the bone marrow cavity, a dough of a cement (control cement or PMMA-1 wt./wt.% $Zn_{0.3}Fe_{2.7}O_4$-loaded cement) was injected into the cavity along the bone hole, and, then, the hole was sealed with bone wax. Following that, the limb was subjected to an AMF (AF = 10-14 kA m^{-1} (126-176 Oe); f = 430 kHz) for 30 min. After exposure to the field, some thinning of the cortical bone in the treated limb was observed but the tibial shape was maintained. μCT results showed that bone volume in the tibia exposed to the magnetic field was significantly higher than that in both the untreated MNPBC group (no exposure to magnetic field) and the control cement group (no exposure to magnetic field), indicating, it was suggested, that exposure to the magnetic field inhibited bone resorption.

The fourth study involved use of the same New Zealand White rabbit tibial plateau tumor model (VX2 solid tumor mass) [25], as was used in the third study. After the rabbit was anesthetized, minced pieces of the tissues of the tumor were injected into the muscles of its right hind leg; and, after the tumor volume reached ~100 mm^3 (after 20 d), the tumor mass model was created by making an incision of the skin at the knee joint, drilling a small hole on the tibial plateau, implanting a small rod of the cement (control cement or 0.2 wt./wt.%$Zn_{0.7}Fe_{2.3}O_4$ MNPs-loaded cement) into the bone marrow cavity, implanting very small fragments of the tumor mass into cavity of the proximal cavity close to the tibial tubercle, sealing the hole with short rod of the cement, and, then, suturing the wound. The leg of the rabbit was then exposed to AMF (AF = 7 kA m^{-1} (88 Oe); f = 380 kHz) 30 min per day for 4 consecutive days. CT scans showed 1) with the control cement, marked cortical bone destruction was present 14 d after exposure to the magnetic field, with complete destruction 28 d after application; and 2) with the MNPBC formulation, 4 d after exposure to the magnetic field, cortical bone appeared to be complete (no obvious damage to the normal bone tissue). Kaplan-Meier survival curves showed markedly longer median survival time for the rabbits in the MNPBC formulation group (~81 d) compared to that in the control cement (~31 d).

5. SHORTCOMINGS OF THE LITERATURE AND AREAS FOR FUTURE STUDY

Thirteen shortcomings of the literature and the associated areas for future study are presented.

First, only four MNPs have been used, namely, Fe_3O_4, SC45, $Zn_{0.3}Fe_{2.7}O_4$, and Fe_2O_3 + TiO_2. A literature shortcoming is that among the studies involving these MNPs, there are those in which characterization of their magnetic properties was not reported (Fe_3O_4 powder + SiO_2 powder [55] or Fe_3O_4 particles [17, 20] or $Zn_{0.3}Fe_{2.7}O_4$ NPs [24]). In future studies, this deficiency should be rectified. In addition, in these studies, the number of MNPs studied for loading into PMMA bone cement for consideration for use in local MHT should be expanded to include novel MNPs and nano-sized entities. Examples of two categories of these materials are presented. In the first category are those whose magnetic characteristics and/or heat-production performance have been reported. Examples are an assembly of g-Fe_2O_3 NPs in the core and an amorphous SiO_2 shell [66], an assembly of SiO_2-coated superparamagnetic γ-Fe_2O_3 NP clusters (SNCs), nanochains (assembled from SNCs), nanobundles (assembled from nanochains) [67], NP clusters comprising an assembly of $CoFe_2O_4$ [68], $MnFe_2O_4$ [68], Fe_3O_4 nanospheres and nanocubes [69], core@shell $CoFe_2O_4$@$MnFe_2O_4$ [70], CdSe NP [71], $CuFe_2O_4$ [72], $La_{0.75}Sr_{0.25}MnO_3$ [73], superparamagnetic iron oxide NPs with surface ligand (provided by a coating of oleic acid and cysteamine acid) [74], $Ni_{1-x}Zn_xFe_2O_4$ [75], angle-shaped superparamagnetic iron oxide NPs [76], $CoFe_2O_4$-$CaFe_2O_4$ and $CaFe_2O_4$-$CoFe_2O_4$ core-shell NPs [77], monodisperse Fe/SiO_2 NPs with core@shell structure [78], citrate- and carboxymethyl cellulose-coated Fe_3O_4 [45], $BaFe_{12}O_{19}$ [79], $(CoFe_2O_4)_x/(Ni_{0.8}Zn_{0.2}Fe_2O_4)_{1-x}$ ($0.2 \leq x \leq 0.8$) [80], dextran-coated $Cu_xFe_{3-x}O_4$ (x = 0.15, 0.31, and 0.47) [81], Eu-doped magnetite [82], $Ba_2Co_2Fe_{12-x}Cr_xO_{22}$ [83], core@shell nanostructure of NiO@Fe_3O_4 [84], an electrospun polyacrylonitrile (PAN) nanofiber mat [85], NiFeMo [86], mesoporous Fe_3O_4 [87], $Mn_xFe_{3-x}O_4$ (x = 0, 0.3, 0.7) [88], multi core-shell Fe_3O_4@SiO_2@β-$NaGdF_4$:RE^{3+} (RE = Ce, Tb, Dy) [89]; $CoFe_2O_4$-$CaCo_3$ [90]; "green" Fe_3O_4 NPs (NPs synthesized from a *Rhus coriaria* extract [91], or *Plantago major* leaf extract [92] or *Tamarindus Indica* seeds [93]); and "green" 47 wt./wt% Fe_3O_4 + 53% wt./wt.% Fe_2O_3 NPs synthesized from orange waste [94]. In the other category are novel MNPs and nano-sized entities whose magnetic characteristics or heat-production performance have not been reported. Examples are $CuCo_2O_4$ NP [95], magnetic ferrite nanocubes/star-like NPs [96], and core-shell nanocomposites (for example, iron oxide core and silica shell [97] and $CoFe_2O_4$ core and

$CoFe_2$ shell [98]), and surface-modified Zn-Mg nanoferrite ($Zn_{0.25}Mg_{0.75}Fe_2O_4$) with an inorganic core and an organic shell [99]).

Second, characterization studies of MNPs should be expanded to include determination of the influence of important variables on key properties that are relevant to local MHT but, which, to date, either have been the subject of only a few studies or have not been reported in the literature. Examples of influencing factors are MNP size, MNP concentration (amount of MNPs in an aqueous solution, for example, of water or agarose), magnitude of the applied magnetic field, and frequency of the applied magnetic field. Examples of underreported or unreported relevant properties are chemical states, magnetic anisotropy coefficient [100], local atomic states [58], and cation oxidation states [25].

Third, there are a number of deficiencies to do with the selection of the control bone cement, preparation of the MNPBC, and *in vitro* characterization of the MNBC. Five of these are highlighted. One, an improved control bone cement formulation was not used in any of the studies. The many shortcomings of current-generation PMMA bone cements are well known, such as high T_{max} (and, hence, high potential for thermal necrosis of peri-treated tissues), susceptibility to premature fracture arising from the radiopacifiers used in the preponderance of formulations ($BaSO_4$ or ZrO_2) acting as stress risers in the cured cement, a large volumetric shrinkage upon polymerization (V_{shr}), bioinertness, suboptimal elution of loaded antibiotics in antibiotic-loaded bone cements (ALBCs), and antibiotics in ALBCs that provide very limited action against a variety of bacteria that are involved in prosthetic joint infection (an example being *S. aureus*). Thus, the literature on PMMA bone cement contains many reports on a large number of improved formulations, examples being formulations that include a phase change material for reducing T_{max} [101], formulations that contain a radiopacifier other than $BaSO_4$ or ZrO_2 [102, 103], formulations that include an additive that results in reduced V_{shr} [104], bioactive formulations [104, 105], microencapsulation of an antibiotic in an ALBC [106], novel antibiotics for incorporation into a new generation of ALBCs [107, 108], and antibiotic-free antimicrobial formulations [109]. In future studies, the control cement used should be an improved formulation. Two, except in one study [20], information on the method used to blend the magnetic nanoparticles with the powder of the control cement is lacking. Three, in one study, the method used to determine t_{set} of the cements (the Vicat needle method [12]) was inappropriate because this method should only be used for calcium phosphate bone cements. In future studies, cement properties should be determined in accordance with protocols given in approved testing standards for PMMA bone cement (for example, ISO 5833 [60] and ASTM F451 [110]). Four, many important investigations have not been performed, such as determination of the influence of coating on an MNP on the heat-generation performance of the cement. Five, with respect to mixing the powder blend (control cement powder + MNPs) and the liquid ("cement preparation method"), either the information is not stated in many reports [12, 13, 14, 15, 16, 18, 19, 20, 22, 24, 26] or manual method was employed, using a spatula [21] or a stirrer [25]. At the moment, there are no approved PMMA bone cement brands for local MHT of bone tumors and, as such, there is no accepted protocol for preparing the cement. Nonetheless, it is recommended that in future local MHT studies, the cement preparation method should be the same as used for arthroplasties. Thus, for *in vitro* studies, the cement should be vacuum mixed, test specimens cured in PBS, at 37 ^{o}C, for 24 h prior to characterization, and determination of t_{set}, T_{max}, compressive strength, compressive modulus, flexural strength, and flexural strength be carried out in accordance with relevant testing standards (namely, ISO 5833 [60] or ASTM F451 [110]).

Fourth, there are studies in which 1) the magnetic properties of the MNPBC were not determined [17, 23, 24, 55]; and 2) the heat-generation performance of the MNPBC was not determined [23, 55]. Future studies should address these shortcomings and, furthermore, be expanded to include determination of 1) the suitability of an MNPBC for observation under typical conditions used in imaging of tumor-bone construct, such as MRI [26], positron emission tomography (PET), and combined PET-MRI; and 2) the influence of a large assortment of variables on *in vitro* properties of an MNPBC that are relevant to its use in direct local MHT but which either have attracted little attention or have not been reported. Examples of such variables are method of synthesis of a given MNP (for example, in the case of Fe_3O_4 MNPs, co-precipitation versus an oxidative aqueous precipitation process versus a microwave hydrothermal process versus a solvothermal process versus a bromide-assisted polyol method versus a surfactant-assisted combustion process versus a green sol-gel combustion process), hydrodynamic size of the MNPs, size distribution of the MNPs, shape anisotropy of the MNPs, and magnitude, frequency, and duration of the applied magnetic field. Examples of such *in vitro* properties are heat-generation performance, injectability, radiopacity, residual monomer content, flexural strength, flexural modulus, specific absorption rate (SAR) (or specific loss power (SLP) or intrinsic loss power (ILP)) [13, 27, 35, 100, 111, 112], spatial distribution of T_{surf}, at a given time during a heat-generation performance test, fatigue life under flexural loading and under torsional loading, and fatigue crack propagation resistance under flexural loading and under torsional loading. This vast trove of results should lead to empirical relationships that delineate the relationship between each of the properties determined and the test variables (taken individually or, preferably, conjointly). In turn, such a relationship would be indispensable in establishing optimum values of the variables that, in turn, will lead to identification of the optimum applied magnetic field dose (field, frequency, and duration) to use in direct local MHT. Use of this dose should result in increased attractiveness of direct local MHT; specifically, simultaneous increase in clinical efficacy and decreased cost.

Fifth, only a very limited amount of *ex vivo* work (five studies) have been reported [17, 18, 20, 25, 55]. In four of these studies, justification was not provided for the use of the model (beef vertebra [17], bovine liver [18, 20] and pig rib [25]). This omission means that the extent to which the results obtained could inform or guide future clinical work is unclear. In future studies, models must be selected carefully.

Sixth, only four studies involving animal bone tumor models have been reported and, among these studies, only two such models have used, these being the nude mouse human breast cancer xenograft [18] and the rabbit tibial plateau with a VX2 solid tumor mass model [20, 24, 25]. Clearly, in the context of bone tumors, justification for the use of the former model must be provided. This paucity of studies on this topic means that is there is scope to expand the variety of such models to include, for example, bone sarcoma mouse model, bovine spinal metastatic tumor model, and murine model. Future work should include 1) three-dimensional maps of temperature (T)-versus-time of application of the magnetic field (t) for the cement, the tumor, and adjacent tissues; 2) morphology of the peri-tissue prior to and after application of the magnetic field; 3) morbidity-free survival profile for the animal; and 4) influence of intrinsic and extrinsic factors on the T-versus-t profile. Examples of intrinsic factors are the size, magnetocrystalline anisotropy, and shape anisotropy of the MNPs, whereas examples of extrinsic factors are the magnitude of the applied magnetic field and duration of its application.

Seventh, in determining the heat-generation performance of MNPBs, only an alternating continuous-mode magnetic field and well-established temperature measurement systems (such as a fluoroptic/fiber optic thermometer or digital thermocouple or far-infrared thermometer) have been used [12, 13, 14, 18, 19, 20, 21, 22, 24]. In future work, emerging systems or sub-systems, such as ultrasound shear wave imaging [113], an intermittently-applied magnetic field system [38], an ultra-short pulse wave magnetic field application system [114], wireless temperature monitoring [115], and a temperature control device for the alternating magnetic field equipment [116, 117], should be used.

Eighth, it is difficult to compare results presented in different literature reports, this being a consequence of differences in a large assortment of features of the studies, among which are how the composition of a cement is reported and, most importantly, the AMF conditions used. Thus, there is urgent for a testing standard for MNPBCs intended for use in local MHT. Examples of protocols that should be included in the standard are methods for preparation of the MNPs, the method and operational details of blending the MNPs with the powder of the control cement (for example, vibratory/vortex mixer, 3000 rpm, for 30 min [20], or magnetically-assisted impaction mixing [118] or mechanofusion [118]), method of mixing the blended powder mixture and the liquid of the control cement (for example, vacuum mixing (evacuation pressure of 72 ± 5 kPa; 1 beat/s; 90 s)), and methods of determination of a large collection of *in vitro* properties of the cement, in particular its heat-generation performance. For the last-mentioned item, it should be ensured that the test conditions are within the safe-limit threshold (that is, the conditions do not result in harm to the patient, such as off-target heating). Three examples of such thresholds are given by Hergt and Dutz [27], Dutz and Hergt [30], Atkinson et al. [119], and Kozissnik et al. [120]. To satisfy this constraint, it is suggested the test conditions used include an applied magnetic field of 20 kA m^{-1} (250 Oe), frequency of 200 kHz, for a time of 30 min.

Ninth, more sophisticated methods should be employed in the characterization of both the MNPs and the MNPBCs to yield enhanced results on, for example, morphology of specimens of as-cured cement and fracture surfaces following a fatigue test. Two such methods are highlighted here. One is dedicated scanning transmission electron microscopy (STEM), coupled with ancillary instrumentation, such as high-angle annular field dark-field (HAADF) or bright-field (BF) or annular bright-field (SABF) detection system and selected area electron diffraction (SAED) [121]. The other is four-dimensional TEM (4D STEM) [122].

Tenth, carefully designed experimental studies on appropriate animal tumor mass models are needed, with the objective being determination of the influence of a host of explanatory variables that are relevant to local MHT on the rate of destruction of the tumor mass (SPP). Examples of variables are size of the tumor mass (d), a thermal property of the tumor mass (for example, thermal conductivity (k)), location of the tumor, concentration of the MNPs in the MNPBC colloidal solution to be applied to the tumor mass (C), magnitude of the applied magnetic field (AF), frequency of the field (f), duration of application of field (t), and temperature rise at the treatment site (DOT). This collection of results should lead to a derived mathematical correlation that links SSP to the collection of explanatory variables used. This derived correlation could be one of the tools used in planning direct local MHT, for a given clinical case.

Eleventh, there is scope for computational studies, of which three examples are given.
One should be analytical and numerical studies of transient heat transfer (conduction and convection) in both the MNPBCs and the tumoral tissues during MHT. A second is the prediction of the heat-generation performance of a MNPBC. For this purpose, machine learning methods (such as Random Forest, K-Nearest Neighbor (KNN), least absolute shrinkage and selector operator (LASSO) regression, Naïve Bayes, and XGBOOST) or deep learning algorithms (such as convolutional neural network, long-short term memory, and RBF network) may be used. The studies could involve determining the predictive performance of individual algorithms or the aggregated/pooled performance of a collection/ensemble of algorithms. The third is magnetization dynamics modeling of direct local MHT as applied to a specified tumor, with such a model considering the relaxation mechanism in the MNPs (for example, coupled Neel and Brownian relaxations)

[48, 111, 112, 123]. These computational studies should facilitate determination of the influence of a large number of both intrinsic and extrinsic explanatory variables, such as size of the MNPs, MNPs concentration in the cement, and frequency of the applied magnetic field, on a vast assortment of properties of the cements. These results could be used for various purposes, such as design of novel MNPBCs, optimization of the process variables involved in direct local MHT using MNPBCs, and planning of direct local MHT, for a given clinical case. These results should be used in conjunction with those outlined above under the Tenth Area for Future Studies.
Although there is acceptance that direct local MHT may have a role in cancer treatment, its approval for such use has been very limited; for example, in 2010, the EMA approved it for use in conjunction with fractionated radiotherapy for treating recurrent glioblastoma multiforme [124]. The results from the studies outlined in Tenth and Eleventh Areas for Future Studies should contribute to local MHT being carried out in in a controlled and repeatable manner which, in turn, may increase the likelihood that many more regulatory bodies will approve direct local MHT for the treatment bone tumors.

Twelfth, magnetic particle imaging (MPI) is an emerging technology that is finding use in many medical fields, such as cancer detection, cardiovascular imaging, and trauma imaging [48, 125, 126, 127]. The principle of this technology may be summarized thus: a gradient field creates a field-free point (FFP) or a field-free line (FFL) and, when an AMF is applied to the treatment site, the MNPs in the FRP or FFL are dynamically energized, thereby inducing a voltage signal [48, 126, 127]. In local MHT, MPI has potential for use in spatial localization of the therapy, resulting in, for example, improved precision and accuracy of the treatment of the target area (tumor mass) and minimization of thermal damage to nontargeted areas [48]. Future studies should investigate the use of MPI when a MNPBC is used in direct local MHT.

Thirteenth, statistical analysis of the quantitative results was reported in only four studies [13, 16, 23, 24] but the presentation was variable. In the first study [13], an inappropriate statistical method (Student's-*t* test) was used. Being a parametric test, the Student's-*t* test should be used only if each of the datasets to be compared is normally distributed. Thus, a test of normality must be performed prior to use of any parametric test of significance. To avoid the extra step of testing for normality, the preferred approach is to use a nonparametric test of comparison, such as the Kruskal-Wallis test or the Mann-Whitney U test. In the second study [16], even though mention was made of the need for normality testing, the specific test used and the results from that test that provided the justification for subsequent use of a parametric test of significance (one-way ANOVA) were not stated in the report. In the other two studies [23, 24], a nonparametric test was used. In all future studies, appropriate statistical methods must be used and all applicable results obtained using these methods should be presented in study reports; for example, use Anderson-Darling or Kolmogorov-Smirnoff normality test followed by use of a parametric test of significance or, else, use a nonparametric test of significance, such as the Kruskal-Wallis test.

6. SUMMARY

The following are the most salient points made in this review:

1. Four magnetic nanoparticles (MNPs) have been synthesized and loaded into PMMA bone cements, producing MNPs-loaded PMMA bone cements (MNPBCs). The MNPs are Fe_3O_4, a glass ceramic (SC45), a combination of Fe_2O_3 + TiO_2, and $Zn_{0.3}Fe_{2.7}O_4$. Thus, the solid phase of an MNPBC comprises a powder phase made up of one of these

MNPs blended with the powder of a control cement and its liquid phase is that of the control cement. It has been proposed that MNPBCs may be suitable for use in one variant of magnetic hyperthermia treatment (herein, designated "direct local MHT") of bone tumors. Characterization of these MNPs included determination of morphology and magnetic properties. Each of these MNPs has excellent magnetic properties.

2. Many formulations of MNPBCs have been prepared and characterized using many tests. Among the *in vitro* properties determined were porosity, setting time (t_{set}), maximum polymerization temperature (T_{max}), compressive strength (σ_c), flexural or bending strength (σ_b), flexural or bending modulus (E_b), magnetization hysteresis profile (magnetization versus coercivity, under a given applied magnetic field), heat-generation performance profile (variation of temperature of the surface of a cement specimen, as a function of time, when subjected to an alternating magnetic field (AMF)), and various measures of cytocompatibility towards both non-tumor and tumor cells. The results for t_{set} (5-16 min), T_{max} (46-90 ^oC), σ_c (60-96 MPa), σ_b (47-72 MPa), and E_b (2.1-2.9 GPa) are within the range specified for PMMA bone cements intended for use in arthroplasties, as given in relevant testing standards, namely, ASTM F451 and ISO 5833 ((3-15 min), < 90 ^oC, > 70 MPa, > 50 MPa, and > 1.8 GPa for t_{set}, T_{max}, σ_c, σ_b, and E_b, respectively). Some of the MNPBC formulations have a suitable heat generation profile, defined as surface temperature reaching 41-45 ^oC over a time that ranged from 0.3-30 min from commencement of application of the magnetic field. It has been postulated that this temperature range is needed to destroy bone tumor cells. Each of the MNPBC formulations was found to be biocompatible/cytocompatible.

3. Various MNPBC formulations have been evaluated in five *ex vivo* tests (lower leg of a human cadaver, excised bovine vertebra, excised bovine liver, and excised bovine rib) for their heat-generation performance when subjected to an AMF. The results showed that the surface temperature at the test site was in the range of 41−45 ^oC, this being achieved in time range of 20 s−35 min.

4. Three MNPBC formulations (6 wt./wt.% Fe_3O_4 MNPs-, 0.2 wt./wt.%$Zn_{0.3}Fe_{2.7}O_4$ MNPs-, and 1 wt./wt.%$Zn_{0.3}Fe_{2.7}O_4$ MNPs-loaded PMMA bone cement formulations) were evaluated in tests using a clinically appropriate animal bone tumor model (New Zealand White rabbit tibial plateau and VX2 tumor mass model). The tests involved subjecting the surgical site to an AMF. Results included temperature at the surgical site of 41−45 ^oC within a time of 0.6−113 min (depending on the magnitude of the applied magnetic field), elimination of the tumor mass, and no bone resorption.

5. Taken together, the collection of results alluded to in items 3) and 4) suggest that as a class of synthetic biomaterials, MNPBC has high potential for use in direct local MHT of bone tumors. In particular, the three formulations alluded to in item 4) are considered leading candidates and, as such, should be the subject of future study.

6. Thirteen shortcomings of the literature are highlighted, with these including lack of information on key aspects of the preparation of the MNPBCs (such as method used to blend the MNPs with the powder of the control cement), wide variability in many test conditions (such as the conditions used in in the determination of the heat-generation performance of a cement), and a very limited number of evaluations of MNPBCs in appropriate animal bone tumor models.

7. The stated literature shortcomings and other considerations suggest thirteen areas for future study, four of which are summarized here. First, evaluation of more MNPs and other nanosized entities for preparing MNPBCs for consideration for use in local MHT. Some of these are currently available, such as $CuFe_2O_4$, electrospun polyacrylonitrile nanofiber + 20 wt./wt.% Fe_3O_4, $Ni_{1-x}Zn_xFe_2O_4$ ($0 \leq x \leq 1$), and Fe_3O nanocubes, while there is opportunity for synthesis of novel ones. Second, use of improved PMMA bone cement formulations (such as bioactive or antibiotic-free variants) as the control cement in a MNPBC. Third, determination of more clinically-relevant properties of MNPBCs, such as radiopacity and fatigue strength. Fourth, performance of computational studies, such as use of a machine learning method to predict the heat-generation performance of an MNPBC specimen when subjected to an AMF.

REFERENCES

1. Kühn K-D. Bone Cements. Springer-Verlag, Berlin, Germany; 2000.
2. Jiranek WA, Hanssen AD, Greenwald AS. Antibiotic-loaded bone cement for infection prophylaxis in total joint replacement. J Bone Joint Surg 2006;88-A:2487-2500.
3. Kühn K-D. PMMA Cements. Springer Medizin, Berlin, Germany; 2014.
4. Lewis G. The properties of acrylic bone cement: state-of-the-art review. J Biomed Mater Res (Appl Biomater) 197; 38:155-182.
5. Ozer D, Er T, Aycan. May bone cement be used to treat benign aggressive bone tumors of the feet with confidence? The Foot 2014;1-5.
6. Duan D-K, Zhang G-C, Sun B-J, Ma T-X, Zhao M. Effect evaluation of denosumab combined with cutterage and bone cement reconstruction in the treatment of recurrent giant cell tumor of bone around the knee joint. Eur Rev Med Pharmocolog Sci 2023;27:5039-5052.
7. Phull SS, Yazdi AR, Ghert M, Towler MR. Bone cement as a local chemotherapeutic drug delivery carrier in orthopedic oncology: a review. J Bone Oncology 2021;6:100345.
8. Goldin AN, Healey RM. The effectiveness and mechanical properties of chemotherapy-impregnated cement in Ewing sarcoma. J Orthop Res 2023;1-7.
9. Wang G, Cui Y, Liu H, Li S, Sun S, Wu D, et al. Antibacterial peptides-loaded bioactive materials for the treatment of bone infection. Colloid Surf B: Biointerfaces 2023; 225:113255.
10. Lewis G. Injectable bone cements for use in vertebroplasty and kyphoplasty: state-of-the-art review. J Biomed Mater Res Part B: Appl Biomater 2006; 76B: 456-468.
11. Quan Q, Gongping X, Ruisi N, Shiwen L. New research progress of modified bone cement applied to vertebroplasty. World Neurosurg 2023;176:10-18.
12. Kawashita M. Kawamura K, Li Z. PMMSA-based bone cements containing magnetite particles for hyperthermia. Acta Biomateriala 2010;6:3187-3192.
13. Li Z, Kawamura K, Kawashita M, Kudo T-a, Kanetaka H, Hiraoka M. In vitro assessment of poly(methylmethacrylate)-based bone cement containing magnetite nanoparticles for hyperthermia treatment of bone tumor. J Biomed mater Res Part A 2012;100A:2537-2545.

14. Tang Z, Wang X, Pan L, Hu Y, Wu Y, Zhang J, Gui S, Kang J, Tang J. Preparation and characterization of PMMA-based cements containing magnetic nanoparticles for the magnetic hyperthermia. Ad Mater Res 2013;647:155-159.
15. Bruno M. Miola M, Bretcanu O, Vitale-Brovarone C, Gerbaldo R, Laviano F. Verne E. Composite bone cements loaded with a bioactive and ferrimagnetic glass-ceramic: Part 1: morphological, mechanical and calorimetric characterization. J Biomater Appl 2014;29:254-267.
16. Verne E, Bruno M, Miola M, Maina G, Bianco C, Cocis A, Rimondini L. Composite bone cements loaded with a bioactive and ferrimagnetic glass-ceramic: leaching, bioactivity and cytocompatibility . Matyer Sci Eng C 2015:C53:95-103.
17. Harabech M, Kiselovs NR, Maenhoudt W, Crevecoeur G, Van Roost D, Dupre L. Experimental ex-vivo validation of PMMA-based bone cements with magnetic nanoparticles enabling hyperthermia of metastatic bone tumors. AIP Advances 2017;7:056704.
18. Ling Y, Tang X, Wang F, Zhou X, Wang R, Deng L, Shang T, et al. Highly efficient magnetic hyperthermia ablation of tumors using injectable polymethylmethacrylate-Fe$_3$O. RSC Adv 2017:7:2913-2918.
19. Miola M, Laviano F, Gerbaldo R, Bruno M, Lombardi A, Cochis A, Rimondini L, Verne E. Composite bone cements for hyperthermia: modeling and characterization of magnetic, calorimetric and *in vitro* heating properties. Ceramics Inter 2017;43:4831-4840.
20. Yu K, Liang B, Zheng Y, Exner A, Kolios M, Xu T, Guo D, et al. PMMA-Fe3O4 for internal mechanical support and magnetic thermal ablation of boner tumors. Theranostics 2019;9:4192-4207.
21. Kubota M, Yokoi T, Ogawa T, Saito S, Furuya M, Yokota K, Kanetaka H, et al. Setting behaviour, mechanical properties and heat generation under alternate current magnetic fields of Fe$_3$O$_4$/TiO$_2$/PMMA composite bone cement. Med Devices Sens 2020;3:e10114.
22. Kubota M, Yokoi T, Ogawa T, Saito S, Furuya M, Yokota K, Kanetaka H, et al. In-vitro heat-generating and apatite-forming abilities of PMMA bone cement containing TiO$_2$ and Fe$_3$O$_4$. Ceramics International 2021;47:12292-1299.
23. Ozdemir F, Evans I, Rankin KS, Bretcanu O. Preliminary evaluation of the *in vitro* biocompatibility of magnetic bone cement composites. Open Ceramics 2021;7:100146.
24. Ren B, Han Z, Liu J. Feasibility study of a novel magnetic bone cement for the treatment of bone metastases. Life 2022;12:1342.
25. Yu X, Gao S, Wu D, Li Z, Mi Y, Yang T, Sun F, et al. Bone tumor suppression in rabbits by hyperthermia below the clinical safety limit using aligned magnetic bone cement. Small 2022;18:2104626.
26. Miola M, Barberis F, Lagazzo A, Verne E. PMMA composite bone cement containing bioactive and ferrimagnetic glass-ceramic particles: effect of temperature and of the additional phase on some physical and mechanical properties. Ceramics International 2023;49:24885-24894.
27. Hergt R, Dutz S. Magnetic particle hyperthermia-biophysical limitations of a visionary tumour therapy. J Magnetism and Magnetic Mater 2007;311:187-192.
28. Dutz S, Hergt R. Magnetic nanoparticle heating and heat transfer on a microscale: basic principles, realities and physical limitations of hyperthermia for tumour therapy. Inter J Hyperthermia 2013; 29:790-800.
29. Hilger I. *In vivo* applications of magnetic nanoparticle hyperthermia. Inter J Hyperthemia 2013; 29:828-834.
30. Dutz S, Hergt R. Magnetic particle hyperthermia−a promising tumour therapy? Nanotechnology 2014:25:452001.

31. Mahmoudi K, Bouras A, Bozec D, Ivkov R, Hadjipanayis C. Magnetic hyperthermia therapy for the treatment of glioblastoma: a review of the therapy's history, efficacy and application in humans. Inter J Hyperthermia 2018;34:1316-1328.
32. Lanier OL, Korotych OI, Monsalve AG, Wable D, Savliwala S, Grooms NWF, Nacea C. Evaluation of magnetic nanoparticles for magnetic fluid hyperthermia. Inter J Hyperthermia 2019;36:686-700.
33. Rodrigues HF, Capistrano G, Bakuzis AF. *In vivo* magnetic nanoparticle hyperthermia: a review on preclinical studies, low-field nano-heaters, noninvasive thermometry and computer simulations for treatment planning. Inter J Hyperthermia 2020;37:76-99.
34. Skandalakis GP, Rivera DR, Rizea CD, Bouras A, Raj JGJ, Bozec D, Hadjipanayis CG. Hyperthermia treatment advances for brain tumors. J Hyperthermia 2020;37: 3-19.
35. Dhar D, Ghosh S, Das S, Chatterjee J. A review of recent advances in magnetic nanoparticle-based theranostics of glioblastoma. Nanomed 2022;17:107-132.
36. Foo CY, Munir N, Kumaria A, Akhtar Q, Bullock CJ, Narayanan A, Fu RZ. Medical advances in the treatment of glioblastoma. Cancers 2022;14:5341.
37. Peiravi M, Eslami H, Ansari M, Zare-Zardini H. magnetic hyperthermia: potentials and limitations. J Indian Chem Soc 2022;99:100269.
38. Tsiapla A-R, Kalimeri A-A, Maniotis N, Myrovali E, Samaras T, Angelakeris M, Kalogirou O. Mitigation of magnetic particle hyperthermia side effects by magnetic field controls. Inter J Hyperthermia 2021;38:511-522.
39. Wlodarczyk A, Gorgon S, Radon A, Bajdak-Rusinek K. Magnetic nanoparticles in magnetic hyperthermia and cancer therapies: challenges and perspectives. Nanomater 2022;12:1807.
40. Farzanegan Z, Tahmasbi M. Evaluating the applications and effectiveness of magnetic nanoparticle-based hyperthermia for cancer treatment; a systematic review. Appl Radiation Isotopes 2023;198:110873.
41. Zhu J, Wang J, Li Y. Recent advances in magnetic nanocarriers for tumor treatment. Biomed Pharmacotherapy 2023;159:11427.
42. Montazersaheb P, Pishgahzadeh E, Jahani VB, Farazadi R, Montazersaheb S. Magnetic nanoparticle-based hyperthermia: a prospect in cancer stem tracking and therapy. Life Sci 2023:323:121714.
43. De Pasquale D, Pucci C, Desii A, Marino A, Debellis D, Leoncino L, Prato M, et al. A novel patient-personalized nanovector based on homotypic recognition and magnetic hyperthermia for an efficient treatment of glioblastoma multiforme. Adv Healthcare Mater 2023:2203120.
44. Rivera D, Schupper AJ, Bouras A, Anatasiadou M, Kleinberg L, Kraitchman DL, Attaluri A, et al. Neurosurgical applicatioins of magnetic hyperthermia therapy. Neurosurg Clin N Am 2023;34:269-283.
45. Vassallo M, Martella D, Barrera G, Celgato F, Coisson M, Ferrero R, Olivetti ES, et al.Improvement of hyperthermia properties of iron oxide nanoparticles by surface coating. ACS Omega 2023;8:2143-2154.
46. Thiesen B, Jordan A. Clinical applications of magnetic nanoparticles for hyperthermia. Int J Hyperthermia 2008;24:467-474.
47. Chang D, Lim M, Goos JACM, Qiao R, Ng YY, et al. Biologically targeted hyperthermia: potential and limitations. Front Pharmacol 2018; 9:831,
48. Le T-A, Hadadian Y, Yoon J. A prediction model for magnetic particle imaging-based magnetic hyperthermia applied to a brain tumor model. Comput Method Programs Biomed 2023;235:107546.
49. Myrovali E, Papadopoulos K, Charalampous G, Kesapidou P, Vourlias G, Kehgias T, Angelakeris M, Wiedwald U. Toward the separation of different heating mechanisms in magnetic particle hyperthermia. ACS Omega 2023;8:12955-12967.

50. American Cancer Society. 2020. Hyperthermia to treat cancer. https:/www.cancer.org/treatment/treatments-and-side-effects/treatment-types/hyperthermi.html
51. Matsumine A, Kasuzaki K, Matsubara T, Shintani K, Satonaka H, Wekabayashi T, Miyazaki S, et al. Novel hyperthermia for metastatic bone tumors with magnetic materials by generating an alternating electromagnetic field. Clin Exp Metastasis 2007;24:191-200.
52. Caizer C. Magnetic/superparamagnetic hyperthermia in clinical trials for noninvasive alternative cancer therapy, In: C. Cazier and M. Rai (editors), Magnetic Nanoparticles in Human Health and Medicine: Current Medical Applications and Alternative Therapy of Cancer; Wiley-Blackwell, Hoboken, NJ, USA; Chapter 18; 2021.
53. Zhu J, Wang J, Li Y. Recent advances in magnetic nanocarriers for tumor treatment. Biomed Pharmocotherapy 2023;159:114227.
54. Siegel RL, Miller KD, Wagle NS, Jemal A. Cancer statistics, 2023. CA Cancer J Clin 2023;73:17-48.
55. Takegami K, Sano T, Wakabayashi H, Sonoda J, Yamazaki T, Morita S, Shibuya T, Uchida A. New ferromagnetic bone cement for local hyperthermia. J Biomed Mater Res (Appl Biomater) 1998;43:210-214.
56. Bretcanu O, Verne E, Coisson M, Tiberto P, Allia P. Temperature effect on the magnetic properties of the coprecipitation derived ferrimagnetic glass-ceramics. J Magnetism Magnetic Mater 2006;300:412-417.
57. Bretcanu O, Verne E, Coisson M, Tiberto P, Allia P. Magnetic properties of properties of the ferrimagnetic glass-ceramics for hyperthermia. J Magnetism Magnetic Mater 2006;305:529-533.
58. Linh PH, Fedotova J, Vorobyova S, Nguyen LH, Huong TT, Nguyen HH, Nguyen TNA, et al. Correlation of phase composition, magnetic properties and hyperthermia efficiency of silica-coated FeCo nanoparticles for therapeutic applications. Mater Sci Eng B 2023;B 295:116571.
59. Burguera EF, Xu HHK, Sun L. Injectable calcium phosphate cement effects of powder-to-liquid ratio and needle size. J Biomed Mater res Part B: Appl Biomater 2008;84:493-502.
60. ISO 5833. Implants for surgery−Acrylic bone cement. International Organization for Standardization, Geneva, Switzerland. 2002.
61. ISO 23317. Implants for surgery−In vitro evaluation of apatite-forming ability of implant materials International Organization for Standardization, Geneva, Switzerland. 2014.
62. Kokubo T, Takadama H. How useful is SBF in predicting in vivo bioactivity? Biomater 2006;27;2907-2915.
63. Saleh H, Seaman LAK, Palmer WC. Proposed dietary recommendations for iron overload: a guide for physician practice. Curr Opinion in Gastroenterology 2023;39:146-149.

64. ISO 10993-5. Biological evaluation of medical devices− Part 5: Tests for in vitro cytotoxicity. International Organization for Standardization, Geneva, Switzerland. 2002.
65. Jang S, Kong W, Zeng H. Magnetotransport in Fe_3O_4 nanoparticle arrays dominated by noncollinear surface spins. Phy Rev B 2007;76:212403.
66. Tadic M, Kralj S, Jagodic M, Hanzel D, Makovec D. Magnetic properties of novel superparamagnetic iron oxide nanoclusters and their peculiarity under annealing treatment. Appl Sur Sci 2014:322:255-264.
67. Kralj S, Makovec D. Magnetic assembly of superparamagnetic iron nanoparticle clusters into nanochains and nanobundles. ACS Nano 2015;10:9700-9707.

68. Makridis A, Chatzitheodorou I, Topouridou K, Yavrapoulou MP, Angelakeris M, Dendinou-Samara C. A facile microwave synthetic route for ferrite nanoparticles with direct impact in magnetic particle hyperthermia. Mater Sci Eng C 2016:C 63:663-670.
69. Nemati Z, Das R, Alonso J, Clements E, Phan MH, Srikanth H. Iron oxide nanospheres and nanocubes for magnetic hyperthermia therapy: a comparative study. J Electronic Mater 2017;46:3764-3769.
70. Suleman M, Riaz S. In silico study of hyperthermia treatment of liver cancer using core-shell $CoFe_2O_4$@$MnFe_2O_4$ magnetic nanoparticles. J Magnetism Magnetic Materials 2020;498:16643.
71. Jafaripour N, Omidvar H, Saber-Samandari S, Mohammadi R, Foroushina RS, Moghadas BK, Soleimani M, et al. Synthesize and. Characterization of a novel cadmium selenide nanoparticle with iron precursor applicable in hyperthermia of cancer cells. Int J Nanosci Nanotechnol 2021;17:77-90.
72. Kurian J, Lahiri BB, Mathew MJ, Philip J. High magnetic field hyperthermia in copper ferrite nanoparticles prepared by solvothermal and hydrothermal methods. J Magnetism Magnetic Materials 2021;538:168233.
73. Zhao S, Zhang K, Zhang Z, Li X, Cai B, Li G. Synthesis and characterization of $L_{0.75}Sr_{0.25}MnO_3$/calcium phosphate composite bone cement with enhanced hyperthermia safety and radiopacity foe bone tumor treatment. J Alloy Compound 2021;888:161544.
74. Mohammad F. Al-Lohedan HA, Joshi PB, Obulapururam PK, Chavali M, Al-Balawi AN, Nikolova MP. Engineered superparamagnetic iron oxide nanoparticles for externally controlled hyperthermia, drug delivery, and therapeutic toxicity. Precise Nanomed 2022;5:930-949.
75. Rabi B, Ounacer M, Essoumbi A, Sajieddine M, Ferreira LP, Costa BFO. Heating efficiency of $Ni_{1-x}Zn_xFe_2O_4$ Magnetic nanoparticles. J Alloy Compound 2023;167241.
76. Kim H, Im PW, Lee C, Hong H, Lee W, Koo C, Park SY, et al. *In vitro* magnetic hyperthermia properties of angle-shaped superparamagnetic iron oxide nanoparticles synthesized by a bromide-assisted polyol method. RSC Adv 2023;13:3803-2810.
77. Vinodhini V, Chintagumpala K. Superparamagnetic hyperthermia and cytotoxicity properties of bimagnetic core-shell nanoparticles synthesized by solvothermal reflux method. J Magnetism Magnetic Materials 2023;565:170290.
78. Qian-Jin S, Ming-Hong D, Hai-Chen C, Xin-Yao, Lu X-G. Preparation and thermogenic performance of monodisperse ferromagnetic/SiO_2 nanoparticles for magnetic hyperthermia and thermal ablation. J Magnetism Magnetic Materials 2023;565:170275.
79. Wagner DV, Kareva KV, Zhuravlev VA, Dotsenko OA, Minin R. Investigation of $BaFe_{12}O_{19}$ hexaferrites manufactured by various syntheses methods using a developed pulse magnetometer. Inventions 2023; 8:26.
80. Rekha K, Vizhi RE. Exploring the structural, magnetic and magnetothermal properties of $(CoFe_2O_4)_x/(Ni_{0.8}Zn_{0.2}Fe_2O_3)_{1-x}$ nanocomposite ferrites. Results in Physics 2023;44:106139.
81. Jamir M, Borgohain C, Borah JP. Dipolar and anisotropy effect on dextran coated Cu doped ferrite for magnetic hyperthermia applications. J Magnetism Magnetic Materials 2023;580:170917.
82. Hazarika KP, Borah JP. Role of site selective substitution, magnetic parameter tuning, and self-healing in magnetic hyperthermia application: Eu-doped magnetite nanoparticles. RSC Adv 2023;13:5045-5057.
83. Suthar M, Khlare D, Gangwar A, Baerjee S, Prasad NK, Dubey AK, Roy PK. Structural, magnetic, and biocompatibility evaluations of chromium substituted

barium hexaferrite (Co_2-Y) for hyperthermia application. Mater Chem Phys 2023;296:127348.
84. Tsopoe SP, Borgohain C, Borah JP. An investigation of inverted core@shell nanostructure for efficacious magnetic hyperthermia applications. Phy Status Solidi A 2023:220:2200801.
85. Mamun A, Sabantina L. Electrospun magnetic nanofiber mats for magnetic hyperthermia in cancer treatment applications−technology, mechanism, and materials. Polymers 2023;15:1902.
86. Muchenski F, Goncalves JP, Ribeiro YC, Franco CRC, de Oliveira CC, Marcon BH, Robert A, et al. Temperature influence on NiFeMo nanoparticles magnetic properties and their viability in biomedical applications. J Biomed Mater Res 2023;111:1488-1498.
87. Shaw SK, Sharma A, Kailashiya J, Gupta SK, Meena SS, Dash D, Maiti P, Prasad NK. Mesoporous Fe_3O_4 nanoparticle: a prospective nano heat generator for thermos-therapeutic cancer treatment modality. J Magnetism and Magnetic Materials 2023;578:170817.
88. Yu X, Yang T, Lv C, Wang L, Liu R, Wu D, Tian D, He S. Cation oxidation states and magnetic properties of $Mn_xFe_{3-x}O_4$ magnetic nanoparticles. J Alloy Compound 2023;937:168291
89. Shrivastava N, Ospina C, Jacinto C, de Menezes AS, Muraca D, Javed Y, et al. Probing the optical and magnetic modality of multi core-shell Fe_3O_4@SiO_2@β-$NaGdF_4$:RE^{3+}(RE = Ce, Tb, Dy) nanoparticles. Optical Mater 2023;137:113585.
90. Choopannezhad S, Hassanzadeh-Tabrizi SA. Synthesis of $CoFe_2O_4$-$CaCo_3$ nanocomposite for simultaneous magnetic hyperthermia and drug release applications. J Alloy Compound 2023;960:170636.
91. Piro NS, Hamad SM, Mohammed AS, Barzinjy AA. Green synthesis magnetite (Fe_3O_4) nanoparticles from *Rhus coriaria* extract: a characteristic comparison with a conventional chemical method. IEEE Trans on Nanobioscience 2023;22:308-317.
92. Lohrasbi S, Kouhbanani N, Beheshtkhoo N, Ghasemi Y, Amani AM, Taghizadeh S. Green synthesis of iron nanoparticles using *Plantago major* leaf extract and their application as a catalyst for the decolorization of azo dye. BioNanoScience 2019;9:317-322.
93. Naik MM, Vinuth M, Kumar VU, Hemakumar KH, Preethi G, Kumar MP, Nagaraju G. A facile green synthesis of nickel ferrite nanoparticles using *Tamarindus Indica* seeds for magnetic and photocatalytic studies. Nanotechnology for Environmental Engineering 2023;8:143-151.
94. Garcia DG, Garzon-Romero C, Salazar MA, Lagos KJ, Campana KO, Debut A, et al. Bioinspired synthesis of magnetic nanoparticles based on iron oxides using orange waste and their application as photo-activated antibacterial agents. Inter J Molecular Sci 2023;24:4770.
95. Ali I, Jamil Y, Khan SA, Pan Y, Shah AA, Chandio AD, et al. Magnetic hyperthermia and antibacterial response of $CuCo_2O_4$ nanoparticles synthesized through laser ablation of bulk alloy. Magnetochemistry 2023;9:68.
96. Gavilian H, Rizzo GMR, Silvestri N, Mai BT, Pellegrino T. Scale-up approach for the preparation of magnetic ferrite nanocubes and other shapes with benchmark performance for magnetic hyperthermia applications. Nature Protocols 2023;18:783-809.
97. Adam A, Mertz D. Iron oxide@mesoporous silica core-shell nanoparticles as multimodal platforms for magnetic resonance imaging, magnetic hyperthermia, near-infrared light photothermia, and drug delivery. Nanomater 2023;13:1342.
98. Nunes MS, da Silva LM, Carrico AS, Morales MA, de Araujo JH. Novel synthesis and physical properties of $CoFe_2O_4$@CoF_2 core@shell nanostructures. Ceramics International 2023;49:24877-24884.

99. Somvanshi SB, Jadhav SA, Gawali SS, Zakde K, Jadhav KM. Core-shell superparamagnetic Zn-Mg ferrite nanoparticles for magnetic hyperthermia applications. J Alloy Compound 2023;947:169574.
100. Nain S, Kumar N, Chudasama B, Avti PK. The SLP estimation of the nanoparticle systems using size-dependent magnetic properties for the magnetic hyperthermia therapy. J Magnetism Magnetic Materials 2023;565:170219.
101. Lv Y, Li A, Zhou F, Pan X, Liang F, Qu X, et al. A novel composite PMMA-based bone cement with reduced potential for thermal necrosis. ACS Appl Mater Interfaces 2015;7:11280-11285.
102. Ayre WN, Scully N, Elford C, Evans BAJ, Rowe W, Rowlands J, et al. Alternative radiopacifiers for polymethyl methacrylate bone cements: silane-treated anatase titanium dioxide and yttria-stabilised zirconium dioxide. J Biomater Appl 2021;35:1235-1252.
103. Xu T-G, Liu D-C, Wang Y, Chen S, Lai B, Zhang F, he J-H. Tungsten carbide-enhanced radiopaque and biocompatible PMMA bone cement and its application in vertebroplasty. Composites Communications 2023;40:101615.
104 Tan Q-C, Jiang X-S, Chen L, Huang J-F, Zhou Q-X, Wang J, et al. Bioactive graphene oxide-functionalized self-expandable hydrophilic and osteogenic nanocomposite for orthopaedic applications. Mater Today 2023;18:100500.
105 Zheng Z, Chen S, Liu X, Wang Y, Bian Y, Feng B, et al. A bioactive polymethylmethacrylate bone cement for prosthesis fixation in osteoporotic hip replacement surgery. Mater Des 2021;209:109966.
106 Sain-Ruiz P, Carbo-Laso E, Del Real-Romero JC, Aran-Ais F, Ballesteros-Iglesias Y, Paz-Jimenez E, et al. Microencapsulation of rifampicin: a technique to preserve the mechanical properties of bone cement. J Orthop Res 2018;36:459-466.
107. Zbornikova E, Gallo J, Vecerova R, Bogdanova K, Kolar M, Vitovska D, et al. Evaluation of second-generation lipophosphonoxins as antimicrobial additives in bone cement. ACS Omega 2020;5:3165-3171.
108. Ghosh S, Sinha M, Samanta R, Sadhasivam S, Bhattacharyya A, Nandy A, et al. A potent antibiotic-loaded bone-cement implant against staphylococcal bone infections. Nature Biomed Eng 2022;6:1180-1195.
109. Lewis G. Antibiotic-free antimicrobial poly (methyl methacrylate) bone cements: a state-of-the-art review. World J Orthop 2022;13:339-353.
110. ASTM F451. Standard specification for acrylic bone cement. American Society for Testing and Materials, West Conshohocken, PA, USA; 2021.
111. Liu NN, Pyatakov AP, Salesky AM, Zharkov MN, Pyataev NA, et al. The “field or frequency” dilemma in magnetic hyperthermia: the case of Zn-Mn ferrite nanoparticles. J Magnetism Magnetic Mater 2022;555:169379.
112. Lemmie OM, Algessair S, Madkhali N, Al-Najar B, El-Boubbou K. Assessing the heat generation and self-heating mechanism of superparamagnetic Fe_3O_4 nanoparticles for magnetic hyperthermia application: the effects of concentration, frequency, and magnetic field. Nanomaterials 2023; 13:453.
113. Lewis MA, Staruch RM, Chopra R. Thermometry and ablation monitoring with ultrasound. Int H Hyperthermia 2015; 31:163-181.
114. Kuwahata A, Adachi Y, Yabukami S. Ultra-short pulse magnetic fields on effective magnetic hyperthermia for cancer therapy. AIP Advances 2023; 13: 025145.
115. Kuwahata A, Hirota R, Sukhbaatar A. Wireless temperature monitoring by using magnetic nanoparticles for biomedical applications on magnetic hyperthermia treatment. AIP Advances 2023;13:025142.
116. Sharma A, Jangam AA, Shen JLY, Ahmad A, Arepally N, Carlton H, et al. Design of a temperature-feedback controlled automated magnetic hyperthermia therapy device.

Front Therm Eng 2023;3:doi:10.3389/fther.2023.1131262.
117. Sharma A, Jangam AA, Shen JLY, Ahmad A, Arepally N, Rodriguez B, et al. Validation of a temperature-feedback controlled automated magnetic hyperthermia therapy device. Cancers 2023;15:327.
118. Wei D, Dave R, Pfeffer R. Mixing and characterization of nanosized powders: an assessment of different techniques. J Nanoparticle Research 2002;4:21-41.
119. Atkinson WJ, Brezovich IA, Chakraborty DP. Usable frequencies in hyperthermia with thermal seeds. IEEE Trans Biomed Eng 1984;BME-31:70-75
120. Kozissnik B, Bohorquez AC, Dobson J, Rinaldi C. Magnetic fluid hyperthermia: advances, challenges, and opportunity. Int J Hyperthermia 2013;29:706-714.
121. Fuertes V, Gregoire N, Labranche P, Gagnon S, Hamada, N Bellanger B, et al. Cubic-shaped and rod-shaped YPO_4 nanocrystal-doped optical fibers: implications for next generation of fiber lasers. App NanoMater 2023;6:4337-4348.
122. Stroppa DG, Meffert M, Hoermann C, Zambon P, Bachevskaya D, Remigy H, et al. From STEM to 4D STEM: ultrafast diffraction mapping with a hybrid-pixel detector. Microscopy Today 2023:31:10-14.
123. Maier-Hauff K, Ulrich F, Nestler D, Niehoff H, Wust P, Thiesen B. Efficacy and safety of intratumoral thermotherapy using magnetic iron-oxide nanoparticles combined with external beam radiotherapy on patients with recurrent glioblastoma multiforme. J Neurooncol 2011;103:317-324.
124. AG, European CE Certificate ("European Certification") and, thus, official approval of NanoTherm®Therapy for the treatment of brain tumors. 2011. Available online at https://www.magforce.com/en/home/for_patients.
125. Wu LC, Zhang Y, Steinberg G, Qu H, Huang S, Cheng M, et al. A review of magnetic particle imaging and perspectives on neuroimaging. Am J Neuroradiol 2019;40:206-212.
126. Healy S, Bakuzis AF, Goodwill PW, Attaluri A, Bulte JWM, Ivkov R. Clinical magnetic hyperthermia requires integrated magnetic particle imaging. WIREs Nanomed Nanobiotechnol 2022;14:e1779.
127. Li Y, Hui H, Zhang P, Zhong J, Yin J, Zhang H, et al. Modified Jiles-Atherton model for dynamic magnetization in x-space magnetic particle imaging. 2023;70:2035-2045.